modelling

MDPI

Article

A Cosserat Mohr–Coulomb Model with Isotropic Hardening and Softening of Cohesion, Friction and Dilatancy for Dense Sand: Laboratory Calibration and Strip-Footing Analyses

Ali Permanoon and Amir Houshang Akhaveissy *

Department of Civil Engineering, Faculty of Engineering, Razi University, Kermanshah 6714414971, Iran; permanoon.ali@gmail.com
* Correspondence: ahakhaveissy@razi.ac.ir

Abstract

Dense sands harden, reach a peak and soften while they dilate; in classical finite element models, this makes the post-peak solution mesh-dependent. This paper presents a plane-strain Cosserat model with the Mohr–Coulomb criterion, a Rankine cut-off and hardening and softening of the friction and dilatancy angles. The multi-surface return uses Fischer–Burmeister functions and a semismooth Newton method with a consistent tangent; it is verified on multi-surface paths, by a patch test and against exact collapse loads. Calibrated on one drained triaxial test on Karlsruhe fine sand, the model predicts four further tests with full-curve errors of 3–5%. For a rough strip footing, the peak pressure converges with mesh refinement, the band width and dissipation are mesh-independent, and the capacity lies 30% below the rigid–plastic solution because the peak strength is mobilised progressively. Stress- and density-dependent peak angles reduce the capacity by 12–26% and cause most of the scale effect. For a footing at a slope crest, the model reproduces ANSYS within 3% in the classical limit; with softening, the classical post-peak response depends on the mesh, whereas the Cosserat response converges.

Keywords: Cosserat continuum; micropolar plasticity; Mohr–Coulomb; strain softening; dilatancy; dense sand; strip footing; bearing capacity; shear localisation; size effect

1. Introduction

The bearing capacity of shallow foundations on sand has been studied for more than a century. The classical solutions of Prandtl [1] and Terzaghi [2], and the semi-empirical superposition formulae of Meyerhof [3] and Vesić [4], assume a rigid–perfectly plastic Mohr–Coulomb material with an associated flow rule. Rigorous values of the self-weight factor N_γ have since been obtained with the method of characteristics [5], finite element limit analysis [6] and displacement finite elements [7]. These studies show that N_γ is highly sensitive to the friction angle and to the roughness of the footing base [6]. They also show that a non-associated flow rule, which is necessary to reproduce the moderate dilatancy of real sands, lowers the collapse load and makes the numerical solution harder to obtain [7]. More recent studies have introduced the stress-level dependence of the friction angle into bearing capacity formulae for sand [8] and have examined the role of fabric anisotropy with coupled material point and discrete element methods [9]. Footings near sandy slopes have been analysed with displacement finite elements [10], advanced constitutive models have been implemented for soil–structure interfaces [11], and large-deformation simulations of

Check for updates

Academic Editors: Ambrosios-Antonios Savvides and Denise-Penelope N. Kontoni

Received: 17 October 2026
Revised: 20 November 2026
Accepted: 22 November 2026
Published: 26 November 2026

Copyright: © 2026 by the authors. Licensee MDPI, Basel, Switzerland. This article is an open access article distributed under the terms and conditions of the Creative Commons Attribution (CC BY) license.

shallow foundations in granular media have been made efficient with hybrid finite element and arbitrary Lagrangian–Eulerian implementations [12].

Real dense sands do not behave as rigid–perfectly plastic materials. In drained shearing they harden, reach a peak friction angle that depends on density and stress level, dilate, and then soften towards a critical state [13,14]. Model tests on dense sand show that this behaviour controls the footing response: failure is progressive, the mobilised friction angle varies along the slip surfaces and the normalised bearing capacity decreases as the footing width increases [15,16]. Part of this scale effect follows from the stress level, because the peak friction and dilatancy angles of a given sand decrease with mean stress [14]. Another part has been attributed to the finite thickness of the shear bands, which is a multiple of the mean grain diameter and therefore does not scale with the footing size [15,16]. Shear bands in dense sand are about 10–20 grain diameters thick, as measured in biaxial tests with stereophotogrammetry and in thin sections [17]. More recent tests with full-field measurements show that the band thickness also evolves with shearing and depends on the grain size distribution [18], and bifurcation analyses relate the onset of shear banding in granular sediments to the change in porosity [19].

Introducing peak strength and softening into a classical continuum model creates a well-known numerical problem. After the peak, the governing equations lose ellipticity, deformation localises in a band whose width is set by the element size, and the load–displacement response and the dissipated energy depend on the mesh [20,21]. Several regularisation techniques have been proposed: non-local formulations, gradient-dependent plasticity and micropolar, or Cosserat, continua [20–22]. These techniques are still being developed and compared, for example implicit gradient enhancements informed by controllability criteria [23], non-local macro–micro damage models [24,25], peridynamic regularisation of soil slope instability [26], rate-dependent regularisation of strain-softening clay [27] and the combination of strong discontinuities with a Cosserat continuum [28]. Engineering practice often avoids the problem altogether: hardening-soil-type models in commercial codes reproduce pre-peak hardening but are normally used without softening [29], while bearing capacity analyses that include softening have to accept mesh-dependent post-peak results [7,16]. For the design engineer, this means that the computed collapse load and the settlement at which it is reached may change when the mesh is refined, and that the reserve capacity of a foundation beyond the peak cannot be assessed reliably. In addition, low-order finite elements are known to overestimate collapse loads of frictional materials with dilatant flow [30,31], so that mesh effects in footing analyses have two sources, localisation and discretisation, which must be distinguished. Strategies to reduce the computational cost of non-linear analyses with localised failure, such as non-linear topology optimisation of the analysed domain, have been proposed for quasi-brittle and masonry structures [32,33], and continuum and discrete descriptions of granular-type failure have been compared [34]. Progressive failure in strain-softening soils remains an active topic in finite element analyses of geotechnical structures [35,36], including subgrade and high-fill slopes [37,38].

The Cosserat continuum, introduced by the Cosserat brothers [39] and later generalised to micropolar elasticity and plasticity [21], adds an independent rotation field and couple stresses to the classical continuum. For granular materials, the additional degree of freedom has a direct physical meaning: the rotation of the grains and the constitutive equations contain an internal length that can be related to the grain size [21,22]. Mühlhaus and Vardoulakis [22] used it to predict the shear band thickness in sand, and de Borst [20] showed that a Cosserat Drucker–Prager model with softening gives mesh-objective shear bands in finite element analyses. Elastoplastic Cosserat models with pressure-dependent yield surfaces and the corresponding return mapping algorithms were later developed for granular soils [40]. Multi-surface Cosserat plasticity has also been used for masonry and

blocky materials [41]. De Borst et al. [42] recently showed that non-associated frictional plasticity can lose ellipticity before any softening, and that a Cosserat continuum restores well-posedness, quadratic convergence of the global Newton method and mesh independence, with a shear band inclination that depends on the internal length. Chang et al. [43] combined micropolar plasticity with non-coaxial flow to study localisation in sand. Other recent Cosserat formulations for granular soils include a micropolar modified Cam-clay model [44], a Cosserat model with evolving fabric anisotropy [45] and Cosserat peripormechanics for localisation and cracking in porous media [46]; Cosserat analyses have also been used for the bearing capacity of anchors in strain-softening soils [36]. Discrete element simulations have quantified couple stresses and grain rotations in granular assemblies, which supports the Cosserat description [47].

A second line of research combined Cosserat kinematics with hypoplasticity [48]. Tejchman and co-workers studied shear band patterning, thickness and wall effects with micropolar hypoplastic models [49]. They also analysed strip footings on sand, including a class A prediction of model tests [50] and deterministic and statistical size effects compared with the tests of Tatsuoka et al. [15,51]. Hypoplastic models describe the dependence on density and pressure in a compact form, but their parameters and incremental non-linearity differ from those of the elastoplastic Mohr–Coulomb framework used by most geotechnical engineers and design codes.

Within elastoplasticity, Panteghini and Lagioia [52] recently formulated a micropolar isotropic plasticity model that covers the Tresca, Mohr–Coulomb, Matsuoka–Nakai and Lade–Duncan criteria through a single family of yield surfaces, with a non-associated flow rule and softening. Their strip-footing analyses showed that, with a non-associated flow rule, the self-weight bearing capacity problem cannot be completed in the classical continuum, whereas the Cosserat continuum gives mesh-independent responses. Panteghini and Rubin [53] proposed a deformable Cosserat formulation in which dissipation is restricted to the macro-continuum, and applied it to a strip footing with a softening friction angle. In neither study were the parameters calibrated on laboratory tests; in the first, softening acts on a single strength parameter, and in the second, the friction angle decreases while the flow rule remains associated. The authors of [53] note that the internal length still has to be identified from experiments.

The integration of a Mohr–Coulomb model with a tension cut-off is demanding in itself: the yield surface has edges and an apex, several surfaces may be active at the same time, and the gradients are discontinuous. Efficient return algorithms in principal stress space are available for the classical continuum [54], and general multi-surface return mapping is described in textbooks [55]. In a Cosserat continuum the stress tensor is not symmetric and couple stresses enter the yield function, so these algorithms cannot be used directly. In addition, the return must remain robust when the friction and dilatancy angles change with the internal variable.

To the authors' knowledge, no elastoplastic Cosserat Mohr–Coulomb model has been published that (i) hardens and softens the cohesion, the friction angle and the dilatancy angle independently with a non-associated flow rule, (ii) is calibrated and checked against drained triaxial tests on a real dense sand, and (iii) has been used to quantify how the internal length affects the load–settlement response, the failure mechanism and the scale effect of a strip footing. The present paper addresses these points. Its main contributions are:

- A plane-strain Cosserat Mohr–Coulomb model with a Rankine tension cut-off, in which c, φ and ψ evolve with one internal variable through peak–residual laws, with optional Rowe [13] and Bolton [14] relations for dilatancy and state dependence;
- A spectral implicit return in which the multi-surface complementarity conditions are written with the Fischer–Burmeister function [56], solved by a semismooth Newton

method with line search and a Levenberg–Marquardt safeguard, and compiled to native code;
- Calibration on a drained triaxial test on dense Karlsruhe fine sand [57], and blind prediction of four further tests at different confining pressures;
- Analyses of a rough rigid strip footing on level ground that compare the classical and Cosserat responses, quantify the effect of l/B on the bearing capacity and on the wedge angle, and separate the Cosserat contribution to the scale effect from the stress-level contribution;
- A comparison with a classical commercial code (ANSYS) on identical meshes for a footing at the crest of a slope, which verifies the implementation and shows the mesh dependence of the classical softening solution and its removal by the Cosserat terms.

The paper is organised as follows. Section 2 presents the Cosserat kinematics, the elastic law, the yield and plastic potential functions and the hardening/softening laws. Section 3 describes the return algorithm and the finite element implementation. Section 4 reports the calibration and validation on triaxial tests. Section 5 presents the strip-footing analyses, and Section 6 compares the model with a classical commercial code for a footing at the crest of a slope. The results are discussed in Section 7, and conclusions are drawn in Section 8.

2. Cosserat Mohr–Coulomb Model with Hardening and Softening

2.1. Kinematics and Static Variables

In plane strain, each material point of a Cosserat continuum has two displacements u_x, u_y and one independent rotation ω_z about the out-of-plane axis [20,22]. The deformation is described by a non-symmetric strain tensor and by two curvatures,

$$\varepsilon_{xx} = \frac{\partial u_x}{\partial x}, \quad \varepsilon_{yy} = \frac{\partial u_y}{\partial y}, \quad \varepsilon_{xy} = \frac{\partial u_x}{\partial y} - \omega_z, \quad \varepsilon_{yx} = \frac{\partial u_y}{\partial x} + \omega_z, \quad \kappa_{xz} = \frac{\partial \omega_z}{\partial x}, \quad \kappa_{yz} = \frac{\partial \omega_z}{\partial y}, \tag{1}$$

with $\varepsilon_{zz} = 0$. The conjugate static variables are the non-symmetric stresses σ_{xx}, σ_{yy}, σ_{zz}, σ_{xy}, σ_{yx} and the couple stresses m_{xz}, m_{yz}. They are collected in the generalised vectors

$$\boldsymbol{\varepsilon} = [\varepsilon_{xx}, \varepsilon_{yy}, \varepsilon_{zz}, \varepsilon_{xy}, \varepsilon_{yx}, l\kappa_{xz}, l\kappa_{yz}]^{\mathrm{T}}, \qquad \boldsymbol{\sigma} = [\sigma_{xx}, \sigma_{yy}, \sigma_{zz}, \sigma_{xy}, \sigma_{yx}, m_{xz}/l, m_{yz}/l]^{\mathrm{T}}, \tag{2}$$

where l is the internal (characteristic) length. Scaling the curvatures and couple stresses by l makes all components dimensionally consistent and preserves $\boldsymbol{\sigma}^{\mathrm{T}}\dot{\boldsymbol{\varepsilon}}$ equal to the stress power.

2.2. Elasticity

The strain is decomposed additively, $\boldsymbol{\varepsilon} = \boldsymbol{\varepsilon}^{\mathrm{e}} + \boldsymbol{\varepsilon}^{\mathrm{p}}$, and the stress follows from linear isotropic Cosserat elasticity, $\boldsymbol{\sigma} = \mathbf{D}^{\mathrm{e}}(\boldsymbol{\varepsilon} - \boldsymbol{\varepsilon}^{\mathrm{p}})$ [20]. In the generalised variables of Equation (2), the elastic matrix is

$$\mathbf{D}^{\mathrm{e}} = \begin{bmatrix} \lambda \mathbf{1}\mathbf{1}^{\mathrm{T}} + 2G\mathbf{I}_3 & \mathbf{0} & \mathbf{0} \\ \mathbf{0} & G\begin{bmatrix} 1+a & 1-a \\ 1-a & 1+a \end{bmatrix} & \mathbf{0} \\ \mathbf{0} & \mathbf{0} & 4G\,\mathbf{I}_2 \end{bmatrix}, \qquad \lambda = \frac{2G\nu}{1-2\nu}, \tag{3}$$

where $\mathbf{1} = [1, 1, 1]^{\mathrm{T}}$. The shear block gives $\sigma_{xy} + \sigma_{yx} = 2G(\varepsilon_{xy} + \varepsilon_{yx})$ for the symmetric part and $\sigma_{xy} - \sigma_{yx} = 2G_c(\varepsilon_{xy} - \varepsilon_{yx})$ for the skew-symmetric part, with the Cosserat shear modulus $G_c = aG$. The last block gives $m_{xz} = 4Gl^2\kappa_{xz}$ and $m_{yz} = 4Gl^2\kappa_{yz}$, i.e., the bending (rotational) stiffness is $4Gl^2$; it is fixed by G and l and involves no further parameter. The elastic Cosserat model thus has the two classical parameters G and ν and two additional parameters, a and l. The ratio $a = 0.5$ is used throughout, as in [20]; because $\varepsilon_{xy} - \varepsilon_{yx}$ is small outside the shear bands, a has little influence on the results: for the reference footing analysis (Q8R, $h = B/16$, $l/B = 0.05$, $c = 0.5$ kPa), $a = 0.25$, 0.5 and 1.0 give peak pressures of 885.6, 889.7

and 892.3 kPa (−0.5% and +0.3%). The internal length l, in contrast, controls the band width (Section 5). Because the stiffness of dense sand increases markedly with the mean stress, the shear modulus is taken from the Hardin-type relation [58]

$$G = G_0\, p_\mathrm{a}\, \frac{(2.17 - e_0)^2}{1 + e_0} \left(\frac{p_0}{p_\mathrm{a}} \right)^{0.5}, \tag{4}$$

with $p_\mathrm{a} = 100$ kPa. G is evaluated from the void ratio e_0 and the mean stress p_0 at the start of shearing (the end of consolidation in the triaxial tests and the gravity state in the boundary value problems), and is then kept constant. G_0 is scaled so that the modulus calibrated for test TMD22 is recovered (Section 4).

2.3. Yield Surfaces

For a symmetric stress state without couple stresses, the Mohr–Coulomb criterion for the pair of principal stresses (σ_i, σ_j) (tension positive) reads

$$f_{ij} = \frac{(\sigma_i - \sigma_j) + (\sigma_i + \sigma_j)\sin\varphi - 2c\cos\varphi}{1 - \frac{1}{3}\sin\varphi} \le 0, \tag{5}$$

where the normalising factor $1 - \sin\varphi/3$ does not change the surface. The six facets $(i, j), i \neq j$, form the hexagonal Mohr–Coulomb pyramid. In the Cosserat continuum, the principal stresses σ_1, σ_2 are those of the symmetric in-plane part of $\boldsymbol{\sigma}$, and $\sigma_3 = \sigma_{zz}$. The skew-symmetric stress and the couple stresses enter through a positive semi-definite quadratic form $\chi = \hat{\boldsymbol{\sigma}}^\mathrm{T} \mathbf{E}\, \hat{\boldsymbol{\sigma}}$, where $\hat{\boldsymbol{\sigma}} = [\sigma_1, \sigma_2, \sigma_3, (\sigma_{xy} - \sigma_{yx})/\sqrt{2}, m_{xz}/l, m_{yz}/l]^\mathrm{T}$ collects the principal stresses and the Cosserat components, and $\mathbf{n}_{ij}(\varphi)$ is the gradient of the deviatoric part of Equation (5) with respect to the principal stresses. Each facet is written as

$$f_{ij} = \sqrt{\left(\mathbf{n}_{ij}(\varphi) \cdot \hat{\boldsymbol{\sigma}}\right)^2 + \chi + \delta^2} - \delta + M(\varphi)\, p - F(\varphi)\, c \le 0, \tag{6}$$

with $M = 2\sin\varphi/(1 - \sin\varphi/3)$, $F = 2\cos\varphi/(1 - \sin\varphi/3)$ and $p = (\sigma_1 + \sigma_2 + \sigma_3)/3$. For $\chi = 0$ and $\delta \to 0$, Equation (6) reduces to Equation (5). The weights in $\mathbf{E}$ follow the usual Cosserat generalisation of J_2 [20,22]; with $(h_1, h_2, h_3) = (3/8, 1/8, 1/4)$ the classical J_2 is recovered for a symmetric stress without couple stresses, and

$$\mathbf{E} = \mathrm{diag}\big(0, 0, 0, 3(h_1 - h_2), 3h_3, 3h_3\big), \qquad \chi = \tfrac{3}{4}\Big[\tfrac{1}{2}(\sigma_{xy} - \sigma_{yx})^2 + (m_{xz}/l)^2 + (m_{yz}/l)^2\Big]. \tag{7}$$

The small regularisation stress δ makes each facet differentiable where $\mathbf{n}_{ij} \cdot \hat{\boldsymbol{\sigma}} = 0$. It is shifted so that $f_{ij}(\mathbf{0}) = -Fc$, which keeps the stress-free state elastic for $c \ge 0$. A value $\delta = 10^{-6}$ kPa is used in all analyses, six to nine orders of magnitude below the stresses of interest; values up to 0.1 kPa change the computed TMD22 response by less than 0.06% (Section 3.3).

Because cohesionless sand cannot carry tension, a Rankine cut-off is added to the three principal stresses,

$$f_k^\mathrm{R} = \sigma_k - f_\mathrm{t} \le 0, \qquad k = 1, 2, 3, \tag{8}$$

with $f_\mathrm{t} = 0$ in all analyses (triaxial and boundary value problems). Without the cut-off, the return of tensile trial stresses to the apex of the Mohr–Coulomb pyramid often has no solution when the dilatancy angle is small or negative, which occurs near the free surface and at the edge of the footing. In a test on stress states sampled from a footing analysis, the local return failed for about 90% of these states without the cut-off and for about 1% with it.

2.4. Flow Rule

The flow rule is non-associated. The plastic potential of each Mohr–Coulomb facet has the form of Equation (6) with φ replaced by the dilatancy angle ψ and without the cohesion term,

$$g_{ij} = \sqrt{\langle \mathbf{n}_{ij}(\psi) \cdot \hat{\boldsymbol{\sigma}} \rangle^2 + \chi + \delta^2} + M(\psi)\, p, \tag{9}$$

where $\langle x \rangle = \max(x, 0)$. The Rankine surfaces are associated. With multipliers $\lambda_{ij} \geq 0$ and $\lambda_k^{\mathrm{R}} \geq 0$,

$$\dot{\boldsymbol{\varepsilon}}^{\mathrm{p}} = \sum_{ij} \dot{\lambda}_{ij} \frac{\partial g_{ij}}{\partial \boldsymbol{\sigma}} + \sum_{k} \dot{\lambda}_k^{\mathrm{R}} \frac{\partial f_k^{\mathrm{R}}}{\partial \boldsymbol{\sigma}}. \tag{10}$$

For one active facet and a symmetric stress without couple stresses ($\chi = 0$, $\delta \to 0$), Equation (9) reduces to $g_{ij} = [(\sigma_i - \sigma_j) + (\sigma_i + \sigma_j) \sin\psi]/(1 - \frac{1}{3}\sin\psi)$, and the flow rule gives the principal plastic strain rates

$$\dot{\varepsilon}_i^{\mathrm{p}} = \dot{\lambda} \frac{1 + \sin\psi}{1 - \frac{1}{3}\sin\psi}, \qquad \dot{\varepsilon}_j^{\mathrm{p}} = -\dot{\lambda} \frac{1 - \sin\psi}{1 - \frac{1}{3}\sin\psi}, \qquad \frac{\dot{\varepsilon}_i^{\mathrm{p}} + \dot{\varepsilon}_j^{\mathrm{p}}}{\dot{\varepsilon}_i^{\mathrm{p}} - \dot{\varepsilon}_j^{\mathrm{p}}} = \sin\psi, \tag{11}$$

with tension and extension positive. Thus, $\psi > 0$ means plastic dilation and $\psi < 0$ plastic contraction, and $\sin\psi$ is the classical ratio of volumetric to shear plastic strain rate [21]. The Macaulay bracket in Equation (9) is active only near the apex. Since $\mathbf{n}_{ij}(\psi) \cdot \hat{\boldsymbol{\sigma}} = [(\sigma_i - \sigma_j) + (\sigma_i + \sigma_j - 2p)\sin\psi]/(1 - \frac{1}{3}\sin\psi)$, on the yield surface $\mathbf{n}_{ij}(\psi) \cdot \hat{\boldsymbol{\sigma}}\,(1 - \frac{1}{3}\sin\psi) = (\sigma_i + \sigma_j)(\sin\psi - \sin\varphi) - 2p\sin\psi + 2c\cos\varphi$, which is positive for every compressive state provided $|\sin\psi| < 3\sin\varphi$ (here $\sin\psi \geq -0.18$ and $\sin\varphi \geq 0.48$). In homogeneous compression tests, the full potential therefore also acts for $\psi < 0$, and the initial contraction of the dense sand is plastic: in the TMD22 simulation, the plastic volumetric strain reaches 0.20% contraction at $\varepsilon_a = 1\%$, against an elastic part of 0.04%. Each multiplier $\dot{\lambda}_{ij}$ is about half the plastic shear strain rate $\dot{\varepsilon}_i^{\mathrm{p}} - \dot{\varepsilon}_j^{\mathrm{p}}$, so in a triaxial test κ is close to the plastic axial strain.

2.5. Hardening and Softening of c, φ and ψ

All three strength parameters depend on one internal variable, the accumulated Mohr–Coulomb multiplier $\kappa = \sum_{ij} \lambda_{ij}$. For each parameter $x \in \{c, \varphi, \psi\}$, a peak–residual law is used:

$$x(\kappa) = \begin{cases} x_0 + (x_{\mathrm{p}} - x_0)\,(2t - t^2), & t = \kappa/\kappa_{\mathrm{p}} \leq 1, \\ x_{\mathrm{r}} + (x_{\mathrm{p}} - x_{\mathrm{r}})\,(1 + \xi)\,e^{-\xi}, & \xi = 2(\kappa - \kappa_{\mathrm{p}})/\kappa_{\mathrm{s}},\ \kappa > \kappa_{\mathrm{p}}, \end{cases} \tag{12}$$

where x_0, x_{p} and x_{r} are the initial, peak and residual values, κ_{p} is the value of κ at the peak and κ_{s} is the softening scale. Equation (12) and its first derivative are continuous at κ_{p}. Its slope is zero at the peak and tends to zero as the residual value is approached. Tabulated laws and constant values can also be used. As alternatives, the dilatancy angle may be linked to the mobilised friction angle by Rowe's stress–dilatancy relation [13],

$$\sin\psi = \frac{\sin\varphi - \sin\varphi_{\mathrm{cv}}}{1 - \sin\varphi\sin\varphi_{\mathrm{cv}}}, \tag{13}$$

and the peak angles may depend on the relative density I_{D} and the mean stress through Bolton's relative dilatancy index [14],

$$I_{\mathrm{R}} = I_{\mathrm{D}}\,(Q - \ln p') - R, \qquad \varphi_{\mathrm{p}} = \varphi_{\mathrm{cv}} + A\,I_{\mathrm{R}}, \qquad \psi_{\mathrm{p}} = B\,I_{\mathrm{R}}, \tag{14}$$

with $I_{\mathrm{R}} \geq 0$ and an upper limit $I_{\mathrm{R,max}}$ (4 in [14]; 8 is used with the constants fitted in Section 4, because the limit 4 would cap φ_{p} below the measured values at low pressure). In the reference model, φ and ψ depend only on κ (Equation (12)), so the influence of the current stress and density enters only through the calibrated peak values. With Equation (14) evaluated from the current mean stress and void ratio of each Gauss point (Section 5.10), the peak angles decrease with increasing stress and with the loosening caused by dilation. The loading direction enters in both variants only through the active facet (Lode angle); non-coaxiality and the dependence on the direction of the strain increment are not represented.

3. Numerical Implementation

3.1. Spectral Return with Fischer–Burmeister Complementarity

The constitutive equations are integrated with the implicit (backward Euler) scheme [55]. Given the committed state and a strain increment, the elastic trial stress is transformed to a spectral basis. Because the in-plane symmetric part is a 2×2 tensor, its eigenvectors are obtained in closed form, and the return is carried out on the principal stresses and the Cosserat components. The unknowns are the stress components in this basis and the nine multipliers $\Delta\lambda_{ij}$, $\Delta\lambda_k^{\mathrm{R}}$. The internal variable is updated as $\kappa_{n+1} = \kappa_n + \sum \Delta\lambda_{ij}$, so the angles and the cohesion are evaluated at the end of the step.

The Kuhn–Tucker conditions $\Delta\lambda \geq 0, f \leq 0, \Delta\lambda f = 0$ of all nine surfaces are replaced by the Fischer–Burmeister equations [56]

$$\phi_{\mathrm{FB}}(\Delta\lambda, -f) = \sqrt{\Delta\lambda^2 + f^2} - \Delta\lambda + f = 0. \tag{15}$$

These equations are semismooth and are satisfied if and only if the complementarity conditions hold. The active set therefore need not be guessed in advance, unlike classical multi-surface algorithms that check the possible combinations of facets [54]. The resulting non-linear system is solved by a semismooth Newton method with an Armijo line search. If the Jacobian is ill-conditioned, a Levenberg–Marquardt step is used instead. The Jacobian includes the derivatives of c, φ and ψ with respect to κ. If the local iteration does not converge, the strain increment is subdivided into 2 to 128 substeps. To make the stress and multiplier unknowns commensurate, the yield functions are divided by the stress scale $S = \max(1\,\mathrm{kPa}, \|\hat{\boldsymbol{\sigma}}^{\mathrm{trial}}\|, c, |f_{\mathrm{t}}|)$ and the multipliers by S/E_s, with $E_s = \max(\|\mathbf{C}\|_2, S)$ the norm of the elastic matrix in the spectral basis. The arguments of ϕ_{FB} are therefore dimensionless and of order one, and the local convergence test $\|\mathbf{r}\| \leq 10^{-10}$ is applied to this scaled residual. The consistent tangent operator is obtained by linearising the converged local system, including the spin terms of the spectral basis. Its verification is reported in Section 3.3.

3.2. Finite Element Formulation and Global Solution

Four-node quadrilaterals with three degrees of freedom per node (u_x, u_y, ω_z) and 2×2 Gauss integration, with a mean-dilatation (B-bar) treatment of the volumetric strain [59] to avoid volumetric locking near the critical state, are used for comparison. Because this element locks in dilatant flow (Section 5.2), the main analyses use eight-node elements with reduced integration (Section 5). The global equations are solved by Newton's method with the consistent tangent and a line search. A step is accepted when the relative force residual, with the rotational degrees of freedom scaled by l, falls below 10^{-6}, or when the displacement correction becomes negligible and the residual is below 10^{-4}. Because the active set can switch between facets near the edges and corners of the yield surface, some steps stagnate at small residuals. Such a step is accepted if its relative residual is below 10^{-3}, which is stricter than the 0.5% force tolerance used by default in common commercial codes. The number of steps accepted in this way is recorded in each analysis.

The point update was first written in MATLAB (R2024b; The MathWorks, Natick, MA, USA) and then compiled with MATLAB Coder. On 1200 randomly generated plastic states, the compiled update reproduced the interpreted one to 10^{-11} (relative) in stress and 5×10^{-11} in the tangent, and it was 19 times faster. Independent analyses were run in parallel on the cores of a workstation.

3.3. Verification of the Implementation

Local return and active sets. Following the practice of verifying finite element solutions in depth against independent results [60], the point update was tested on strain paths that activate the different parts of the yield surface (Table 1), with the parameters of Table 2,

$c = 2$ kPa and $l = 0.05$. Each path starts from an isotropic stress of 100 kPa (20 kPa for the tension paths) and passes through hardening, the peak and softening where applicable. The paths activate a single facet, an edge (two facets), the apex with the Rankine cut-off and the cut-off alone; they also include non-zero couple stresses and skew-symmetric stresses, and very large increments. In all 1018 increments, the local semismooth Newton method converged in at most 17 iterations (5–7 on average) to a scaled residual below 5×10^{-10}, without substepping. The consistent tangent was compared with central, forward and backward finite differences of the stress with respect to all strain components except ε_{zz}, with perturbations $h = (10^{-4} \dots 10^{-9}) \max(10^{-6}, \|\boldsymbol{\varepsilon}\|)$. The median relative error (Frobenius norm) is 10^{-11}–10^{-6}. The largest error, 7×10^{-4}, occurs at a corner where the Rankine surface is active and an MC facet is reached with zero multiplier; there, the response is not differentiable and the analytical tangent is one of the one-sided tangents. The error is equally small at the increments where the active set changes or where κ passes κ_p (column "transitions"). The choice of the perturbation interval is justified in Appendix B by a study of the error as a function of the perturbation size.

Table 1. Verification of the local return on strain paths through different active sets. "Active sets": number of active MC facets + Rankine surfaces, and number of increments. FD error: relative difference between the consistent tangent and the finite-difference tangent.

Path	Incr.	Iter. Max/Mean	Max Residual	Active Sets (Count)	FD Error of Tangent		
					Max	Median	Transitions
Simple shear, hardening–softening	300	13/5.8	8×10^{-11}	1+0:275, 1+1:22, 2+0:2, 2+1:1	1×10^{-6}	4×10^{-11}	2×10^{-9}
Biaxial compression (edge)	200	5/5.0	8×10^{-15}	2+0:181	1×10^{-10}	3×10^{-11}	2×10^{-11}
Volumetric extension (apex)	100	7/6.0	8×10^{-13}	0+2:90, 1+2:6, 2+0:1, 2+2:1	2×10^{-8}	7×10^{-10}	9×10^{-9}
Uniaxial extension (cut-off)	100	6/5.0	6×10^{-12}	0+1:95, 2+0:1, 2+1:2	7×10^{-4}	2×10^{-6}	2×10^{-6}
Shear + rotation + curvature	300	17/5.7	5×10^{-10}	1+0:277, 2+1:7, 2+2:12, other:4	3×10^{-6}	4×10^{-11}	9×10^{-7}
Simple shear, 10 increments	10	8/6.6	2×10^{-11}	1+0:10	5×10^{-10}	4×10^{-11}	–
Biaxial, 8 increments	8	5/5.0	7×10^{-14}	2+0:8	6×10^{-11}	3×10^{-11}	–

Comparison with a classical return. For symmetric stresses without couple stresses, the model reduces to non-associated Mohr–Coulomb plasticity. For perfect plasticity ($\varphi = 35°$, $\psi = 10°$, $c = 5$ kPa), the update was compared with an independent return in principal stress space (return to the plane, to the two edges and to the apex, in the spirit of [54]) for 400 random compressive trial stresses. The principal stresses agree to 10^{-8} (relative) for returns to the plane (185 cases) and to the triaxial-compression and triaxial-extension edges (56 and 60 cases); the remaining 99 trial states were elastic.

Table 2. Model parameters calibrated on test TMD22.

Parameter	Initial	Peak	Residual	$\boldsymbol{\kappa}_p$	$\boldsymbol{\kappa}_s$
Friction angle φ (°)	28.6	42.75	33.3	0.0466	0.18
Dilatancy angle ψ (°)	−10.5	18.6	0	0.0466	0.18
Cohesion c (kPa)	0 (triaxial), 0.25–2 (BVPs)			–	–
$E = 300$ MPa at $p_0 = 100$ kPa, $e_0 = 0.735$ (Equation (4)); $\nu = 0.25$; $a = 0.5$; $f_t = 0$					

Patch test. A patch of four distorted elements (interior node at $(0.42, 0.61)$ in a unit square) was loaded by prescribing on its boundary a linear displacement field and the corresponding rigid rotation. The interior node is reproduced to 10^{-19} m and the Gauss-point stresses are uniform to 10^{-13} kPa in the elastic case, and to 10^{-14} m and 2×10^{-9} kPa when all 16 Gauss points are plastic.

Regularisation stress and global tolerance. For $\delta = 10^{-6}$, 10^{-3}, 10^{-2} and 10^{-1} kPa, the peak deviator stress of TMD22 is 422.66, 422.67, 422.69 and 422.90 kPa; even $\delta = 1$ kPa changes it by only 0.6%. Because δ rounds the facets only where $\mathbf{n}_{ij} \cdot \hat{\boldsymbol{\sigma}}$ and χ are both small, its effect in a boundary-value problem scales with δ/c. For the slope with couple stresses and cohesion softening of Section 6.3 (case B, 20×20 mesh, $l = 0.141$ m, $c = 40$ kPa), $\delta = 10^{-6}$ and 10^{-3} kPa give identical load–settlement curves (peak 589.0 kN/m, 334.6 kN/m at $U = 500$ mm), $\delta = 0.1$ kPa raises them by 0.2–0.5% and $\delta = 1$ kPa ($\delta/c = 0.025$) by 2–5% (Section 6.3). In the boundary-value problems of this paper $\delta/c \leq 10^{-5}$, more than two orders of magnitude below the ratio at which the effect is still only 0.2–0.5%. The global Newton iteration with the consistent tangent also converges quadratically in the boundary-value problems: in the same slope analysis, the relative residual falls, for example, from 3.4×10^{-3} to 2.0×10^{-4} and 1.0×10^{-8}, and every increment converges in at most four iterations (Section 6.3). The footing analysis with $h = B/16$, $l/B = 0.05$ and $c = 2$ kPa (Section 5) was repeated with the acceptance threshold for stagnating steps reduced from 10^{-3} to 10^{-5}: the peak pressure is 1219.1 kPa in both analyses, so that the relaxed criterion does not affect the results.

4. Calibration and Validation on Triaxial Tests

4.1. Experimental Data

The model was calibrated on the drained monotonic triaxial tests on Karlsruhe fine sand reported by Wichtmann and Triantafyllidis [57]. The sand is a poorly graded fine quartz sand ($d_{50} = 0.14$ mm, $e_{\min} = 0.677$, $e_{\max} = 1.054$). Tests TMD21–TMD25 were performed on dense specimens ($I_{D0} = 0.85$–0.95) at effective confining pressures of 50, 100, 200, 300 and 400 kPa. Test TMD22 ($\sigma_3 = 100$ kPa, $e_0 = 0.735$) was used for calibration, and the other four tests were predicted. The complete deviator stress and volumetric strain curves of the five tests were extracted from the vector graphics of the published figure [57]. The curves are stored there as vector paths, so their coordinates were transformed exactly with the axis calibration, without manual digitisation.

The database of Wichtmann and Triantafyllidis contains many monotonic and cyclic tests on this sand, and later studies have examined the effects of drainage conditions, preloading, preshearing and sample preparation [61,62]. The present model describes monotonic drained loading from an isotropic, normally consolidated state with one internal variable. The five drained monotonic triaxial compression tests on dense specimens of nearly equal density are therefore the subset that corresponds directly to the model assumptions and to the footing problem: one dense sand, drained, first loading, at mean stresses of 50–900 kPa. Tests with other paths, cyclic loading or preloading would examine features that the model does not contain; their limits are discussed in Section 7.

4.2. Single-Element Calibration

A single material point was analysed under axisymmetric conditions ($\sigma_{xx} = \sigma_{zz} = -\sigma_3$, $\varepsilon_{xx} = \varepsilon_{zz}$). For a homogeneous state, the curvatures and the skew-symmetric stresses are zero, so the Cosserat terms do not contribute and the calibration is the same as for the classical model. Table 2 lists the parameters. The peak friction and dilatancy angles were determined from the peak deviator stress and the maximum dilatancy rate. The residual friction angle, $\varphi_r = 33.3°$, is close to the critical-state angle reported for this sand (33.1° [57]). The residual dilatancy angle was set to zero, consistent with the critical state.

The calibrated model gives a peak deviator stress of 423 kPa for TMD22, against 410 kPa measured, and an end-of-test deviator stress of 292 kPa, against 294 kPa (Figure 1). The calibrated volumetric response captures the initial contraction and the subsequent dilatancy. The model reaches the peak at an axial strain of 4.3%, while the test peaks at 6.2%. Over the complete curve the normalised root-mean-square error (RMSE divided by the measured peak) is 2.8% for q, and the RMSE of ε_v is 0.55% strain. The peak strain could be matched by increasing κ_p by 45%. However, the full-curve error then rises from 2.8% to 5.9% and the pre-peak error from 4.4% to 10.1%, because the measured curve is much flatter near the peak than the two-parameter hardening branch of Equation (12) allows (Figure 2c). The calibrated κ_p is therefore the best compromise for this law. A third parameter in the hardening branch would be needed to reproduce both the initial stiffness and the peak strain.

4.3. Prediction of Tests at Other Confining Pressures

The four other tests were analysed with the calibrated parameters in four ways (Tables 3 and 4). The first two are genuine predictions because only TMD22 is used: (i) the peak angles are kept constant; (ii) they follow Bolton's relation (14) with his constants $A = 3$ and $R = 1$, with $Q = 10.39$ and $B = 5.9$ fitted to TMD22. (iii) In the third, $A = 1.48$ and $Q = 13.70$ are fitted to the peaks of all five tests; this is an in-sample fit, not a validation. (iv) To validate the fitted relation, a leave-one-out test was performed: for each test, A and Q were fitted to the peaks of the other four tests, and the excluded test was predicted. The elastic modulus followed Equation (4) with the void ratio and confining pressure of each test.

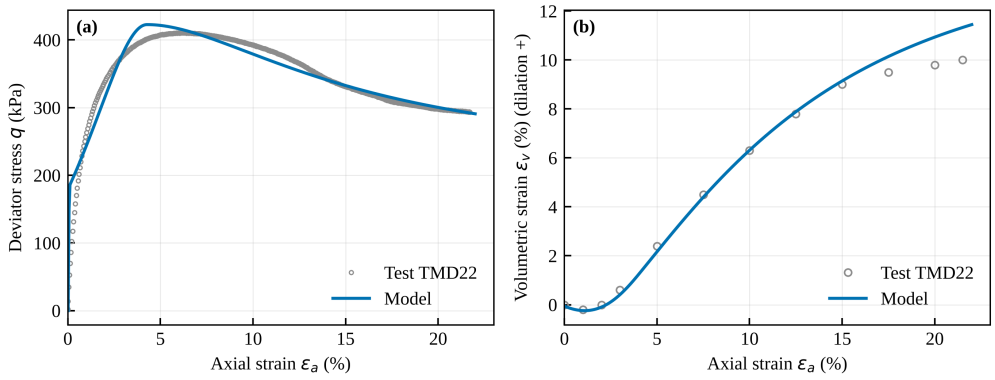

Figure 1. Calibration on test TMD22 ($\sigma_3 = 100$ kPa, $e_0 = 0.735$): (**a**) deviator stress and (**b**) volumetric strain versus axial strain. Test data from [57]; the volumetric data were digitised from the published figure.

Table 3. Peak deviator stress: measured [57] and computed (error in parentheses). (i) and (ii): calibration on TMD22 only; (iii): fit to all five tests (in-sample); (iv): leave-one-out prediction (out-of-sample).

Test	σ_3 (kPa)	Measured (kPa)	(i) Constant Peaks	(ii) Bolton	(iii) Bolton, Fitted	(iv) Bolton, Leave-One-Out
TMD21	50	212.5	211.3 (−0.6%)	233.1 (+9.7%)	214.8 (+1.1%)	223.7 (+5.3%)
TMD22	100	411.3	422.7 (+2.8%)	422.7 (+2.8%)	408.2 (−0.8%)	407.5 (−0.9%)
TMD23	200	843.9	845.3 (+0.2%)	810.5 (−4.0%)	815.9 (−3.3%)	808.4 (−4.2%)
TMD24	300	1223.0	1268.0 (+3.7%)	1161.8 (−5.0%)	1203.3 (−1.6%)	1193.3 (−2.4%)
TMD25	400	1465.3	1690.7 (+15.4%)	1435.9 (−2.0%)	1519.5 (+3.7%)	1572.6 (+7.3%)

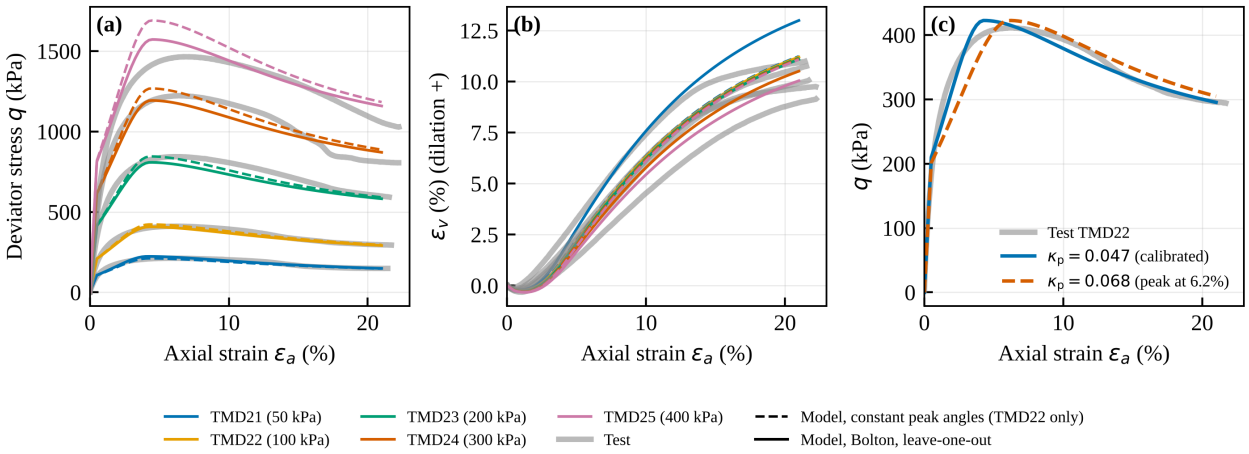

Figure 2. Tests TMD21–TMD25 (thick grey: test curves extracted from [57]): (**a**) deviator stress and (**b**) volumetric strain computed with constant peak angles calibrated on TMD22 (dashed) and with the leave-one-out Bolton relation (solid); (**c**) TMD22 with the calibrated κ_p and with κ_p increased to match the measured peak strain.

Table 4. Errors over the complete curves (ε_a = 0.5–21%): normalised RMSE of q over the whole curve and over the pre-peak part (ε_a below the measured peak strain), RMSE of ε_v, and axial strain at the peak.

	(i) Constant Peak Angles			(iv) Leave-One-Out		$\varepsilon_{a,\mathrm{peak}}$ (%)	
Test	q, **All (%)**	q, **Pre-Peak (%)**	ε_v **(% Strain)**	q, **All (%)**	ε_v **(% Strain)**	**Model**	**Test**
TMD21	4.4	5.4	0.85	3.7	0.89	4.3	5.8
TMD22	2.8	4.4	0.55	3.9	0.55	4.3	6.2
TMD23	4.1	4.1	0.23	6.3	0.21	4.4	6.0
TMD24	4.5	4.8	0.54	5.2	0.30	4.4	6.4
TMD25	9.4	14.3	1.48	5.3	0.78	4.4	6.8

With constant peak angles, the peak error is within 4% up to σ_3 = 300 kPa (mean stress at the peak up to about 700 kPa). It grows to 15% at 400 kPa, where the measured peak friction angle is 2° lower. Over the whole curves the normalised error is 3–5% and the volumetric error 0.2–0.9% strain in this range (Figure 2). With Bolton's original constants, calibrated on TMD22 alone, the peak error is −5% to +10% over 50–400 kPa. The largest error is at 50 kPa, where the relation extrapolates furthest. In the leave-one-out test, the out-of-sample peak errors are −4.2% to +7.3%. The largest errors are again at the ends of the pressure range (50 and 400 kPa), where the excluded test is an extrapolation of the other four. Within the fitted range, Bolton's relation therefore predicts the peak strength to be about 5%. The constant-angle calibration transfers reliably over 50–300 kPa, i.e., for mean stresses at failure up to about 700 kPa at this density.

The footing analyses of Section 5 use the constant TMD22 parameters, so that the effect of the Cosserat internal length can be isolated. At the peak of the Q8R analyses, the mean stress reaches 700–870 kPa in a few elements at the footing edge, but 99% of the elements remain below about 530 kPa and most of the failure mechanism below 300 kPa, i.e., mainly inside the range where the constant parameters are validated. The effect of stress- and density-dependent peak angles on the footing is studied separately in Section 5.10.

5. Rough Rigid Strip Footing on Dense Sand

5.1. Model

A rigid rough strip footing of width B on level ground was analysed with a half model (Figure 3). The domain is 12B wide and 5B deep, which contains the Prandtl mechanism

of the peak friction angle (it reaches about $10B$ from the axis and $2.7B$ in depth). On the symmetry axis $u_x = 0$ and $\omega_z = 0$. The base is fixed, and the far side has $u_x = 0$. The mesh is structured. Elements of size h fill a zone of $4B \times 2.5B$ under and beside the footing, and outside this zone the element size grows geometrically to $B/2$. Five refinements, $h = B/8$, $B/12$, $B/16$, $B/24$ and $B/32$, were used (1590 to 15,386 elements). Two element types were used: the four-node quadrilateral with B-bar treatment described in Section 3 (Q4), and an eight-node serendipity element with the same three degrees of freedom per node and 2×2 reduced integration (Q8R) [31], which is known to perform better in limit-load problems with frictional, dilatant materials. The footing nodes have $u_x = 0$ and $\omega_z = 0$ (rough, rigid base) and a uniform prescribed settlement s. The footing pressure is $q = 2Q/B$, where Q is the reaction of the half footing.

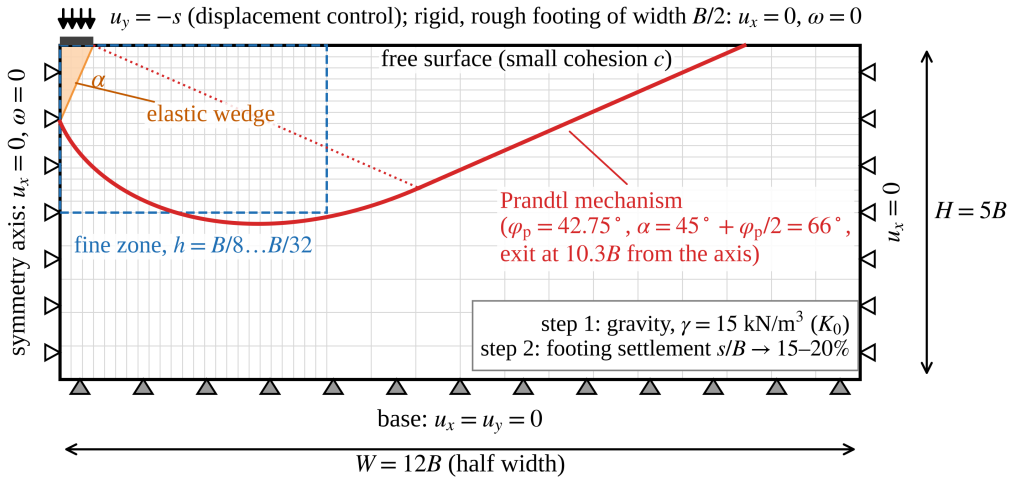

Figure 3. Half model of the rough rigid strip footing: geometry, boundary conditions, structured mesh with refined zone, and the Prandtl mechanism for $\varphi_p = 42.75°$. Open triangles: roller supports ($u_x = 0$) on the symmetry axis and the lateral boundary; grey triangles: fixed base ($u_x = u_y = 0$).

The analysis has two steps. In the first, an elastic gravity analysis ($\gamma = 15$ kN/m^3) gives the initial stresses. Because the base is fixed and $u_x = 0$ on the axis and on the far side, the lateral strain vanishes and the gravity state is geostatic, $\sigma_{yy} = -\gamma|y|$, with $\sigma_{xx} = \sigma_{zz} = K_0\sigma_{yy}$ and $K_0 = \nu/(1-\nu) = 0.33$, close to Jaky's estimate $1 - \sin\varphi_p = 0.32$ for the dense sand. These are used to assign the elastic moduli (Equation (4), eight classes of p_0), and the gravity stresses are then installed as initial stresses and equilibrated with the elastoplastic model. In the second, the footing is pushed down to $s/B = 20\%$ with an adaptive step size. The strength parameters are those of Table 2, i.e., exactly the values validated in Section 4. A small cohesion keeps the zero-stress state at the free surface away from the apex of the yield surface. Without it, the points beside the footing reach the apex, where the MC pyramid and the Rankine cut-off meet and the rotational stiffness vanishes, and the global iteration fails within the first increments. The main analyses use $c = 0.5$ kPa; analyses with $c = 2$ kPa are also reported, and the influence of c is quantified in Section 5.5. The internal length was varied as $l/B = 0.005$ (practically classical, $l/h \leq 0.08$), 0.01, 0.025, 0.05 and 0.1, with $B = 1$ m.

5.2. Benchmarks with Known Collapse Loads

Before the sand analyses, the footing model was checked against two problems with known collapse loads, using perfectly plastic materials with constant parameters (Table 5). For an almost purely cohesive soil ($\varphi = \psi = 1°$, $c = 20$ kPa, $\gamma = 15$ kN/m^3), the exact solution is $q_u = cN_c = 107.6$ kPa. The computed collapse pressures with $l = 0.05$ m are

126.6 kPa (Q4, $h = B/16$) and 129.4 kPa (Q8R, $h = B/8$). With $l = 0.005$ m they converge monotonically with refinement (Figure 4a): 119.2, 114.5 and 113.0 kPa for Q8R with $h = B/8$, $B/16$ and $B/24$, and 114.3 kPa for Q4 with $h = B/32$. The Richardson extrapolation of the Q8R results gives 110.3 kPa (convergence order 1.1), 2.5% above the exact value. The remaining difference is typical of a stress singularity at the edge of a rough footing.

The second benchmark is the classical N_γ problem for an associated material ($\varphi = \psi = 30°$, $c = 0.5$ kPa, rough base). The exact value of Martin [5], $N_\gamma = 14.75$, gives $q_u \approx \frac{1}{2}\gamma B N_\gamma + cN_c = 111 + 15 = 126$ kPa. With the internal length used in the sand analyses ($l = 0.05$ m), the computed pressures are much higher: 418, 321 and 259 kPa for Q4 with $h = B/8$, $B/16$ and $B/32$, and 241, 222 and 215 kPa for Q8R with $h = B/8$, $B/16$ and $B/24$. Three contributions were separated by additional analyses (Figure 4b). (i) The Cosserat length: with $l = 0.005$ m the Q8R pressure on the $B/8$ mesh drops from 241 to 179 kPa, and with $l = 0.001$ m a further 4% on the $B/24$ mesh. In this shallow, self-weight-dominated mechanism, the rotation gradients at the footing edge are large, and $l/B = 0.05$ raises the collapse load by about one third. (ii) The element: with $l = 0.005$ m, the Q4 pressures (362, 271 and 208 kPa for $h = B/8$, $B/16$, $B/32$) rise continuously with settlement without reaching a limit, which is the typical locking response of low-order elements in dilatant plastic flow [30,31]. The Q8R analyses reach a clear limit load that converges with refinement: 178.5, 163.7, 160.0 and 158.2 kPa for $h = B/8$, $B/16$, $B/24$ and $B/32$, i.e., about 154 kPa by Richardson extrapolation. (iii) The cohesion: with $c = 0.1$ kPa the Q8R pressures are 140.7 and 136.7 kPa ($B/16$, $B/24$). The computed cohesion term is therefore about 58 kPa per kPa, compared with $N_c = 30$, because the self-weight and cohesion terms do not superpose exactly. Removing the cohesion term (linear extrapolation to $c = 0$) and the remaining effect of l from the extrapolated Q8R value gives $q_u \approx 118$ kPa, i.e., $N_\gamma \approx 15.7$, 7% above Martin's exact value of 14.75. The non-associated case ($\psi = 0$) gives 195 kPa (Q4, $h = B/16$, $l = 0.05$ m) and 205 and 187 kPa (Q8R, $h = B/8$ and $B/16$, $l = 0.05$ m), consistent with these findings. Low-order elements are known to overestimate collapse loads for frictional materials with dilatant flow, because the volumetric constraint imposed by the flow rule cannot be satisfied by enough independent kinematic modes [30,31]. With 15-node triangles and carefully refined meshes, N_γ is reproduced within about 5% for $\varphi = 30°$ [63].

The benchmarks therefore verify the implementation: the purely cohesive problem converges to within 2.5% of the exact value, and the frictional problem converges to within 7% once the Cosserat and cohesion contributions are removed. They also have two consequences for the sand analyses. First, the Q4 element is not suitable for the frictional, dilatant footing problem. The main analyses therefore use Q8R; the Q4 capacities ($h = B/16$) overestimate the converged values (Section 5.3). Second, with internal lengths of a few percent of B, the Cosserat continuum adds a significant strength in the footing problem. This effect is part of the model response and is discussed in Section 7.

Table 5. Benchmarks with known collapse loads (rough rigid strip footing, $B = 1$ m, $\gamma = 15$ kN/m^3, $l = 0.05$ m): computed and exact collapse pressure (kPa). Results with smaller l are given in Figure 4.

Material	Exact	Q4, $B/8$	Q4, $B/16$	Q4, $B/32$	Q8R, $B/8$	Q8R, $B/16$
$\varphi = \psi = 1°$, $c = 20$	107.6	–	126.6	–	129.4	–
$\varphi = \psi = 30°$, $c = 0.5$	126	418	321	259	241	222
$\varphi = 30°$, $\psi = 0$, $c = 0.5$	$\approx$105 [a]	–	195	–	205	187

[a] $N_\gamma \approx 12$ for $\psi = 0$ from refined finite element analyses [63], plus cN_c.

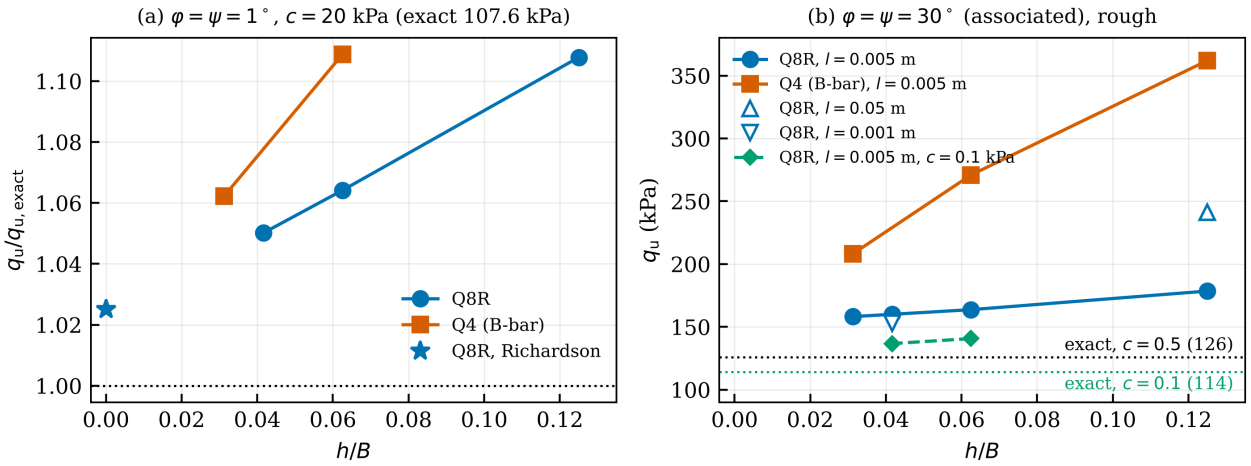

Figure 4. Benchmarks with known collapse loads: (**a**) near-Tresca soil, ratio of computed to exact collapse pressure versus element size; (**b**) associated N_γ problem: collapse pressure versus element size for Q4 and Q8R elements and different internal lengths and cohesions. Dotted lines: exact values.

5.3. Mesh Convergence at Fixed Internal Length

The mesh dependence was studied at a fixed internal length, so that the ratio l/h increases with refinement (Table 6, Figure 5). With the Q4 element ($l/B = 0.1$, $c = 2$ kPa), the peak pressure decreases steadily from >1680 kPa ($h = B/8$, no peak) to 1406, 1255, 1153 and 1109 kPa for $h = B/12$, $B/16$, $B/24$ and $B/32$. The decrease slows down but has not ended at $l/h = 3.2$. The Q8R element gives much smaller differences: 1266 (no peak), 1208 and 1173 kPa for $h = B/8$, $B/12$ and $B/16$. With the reduced cohesion $c = 0.5$ kPa, the Q8R peak pressures for $l/B = 0.05$ are 976, 921, 890 and 859 kPa for $h = B/8$, $B/12$, $B/16$ and $B/24$. A Richardson extrapolation of the three finest meshes (order 1.0) gives $q_{max} \approx 800$ kPa, so the $B/16$ value is about 11% above the converged estimate. For $l/B = 0.1$, the values are 1056, 985 and 953 kPa ($h = B/8$, $B/12$, $B/16$).

The pre-peak response, the settlement at the peak ($s/B = 15$–18%) and the global measures of the localised deformation converge much faster than the peak pressure (Table 6). The plastic dissipation, computed from the energy balance $D = W_{ext} + W_\gamma - \Delta U_{el}$ (external work of the footing, work of gravity, change in elastic energy), is 20.5, 20.9 and 19.9 kJ/m at $s/B = 10\%$ and 64.3, 61.2 and 59.7 kJ/m at $s/B = 20\%$ for $h = B/8$, $B/12$ and $B/16$ ($l/B = 0.05$). The shear band that bounds the wedge (Section 5.9) has a thickness of 0.42, 0.38 and 0.39 m on the three meshes. It was measured as the full width at half maximum of the post-peak increment of κ, normal to the band. The width of the localised zone is therefore controlled by l and not by h, as expected for the regularised continuum, while the limit pressure converges more slowly because of the singular stress field at the edge of the rough footing (Section 5.2). The classical limit could not be studied in the same way. With $l/B = 0.01$ ($l/h = 0.08$–0.24), the analyses stalled at $s/B = 4.0\%$, 3.5%, 3.5% and 4.5% on the $B/8$, $B/12$, $B/16$ and $B/24$ meshes, when narrow bands one to two elements wide formed under the footing edge, long before the peak at $s/B \approx 15\%$. A direct comparison with a classical continuum is therefore made on a second example (Section 6).

Table 6. Mesh convergence at fixed internal length: peak pressure q_{max} (kPa), settlement at the peak and plastic dissipation D at s/B = 10% and 20% (kJ/m, half model). l/h: number of elements per internal length.

Element, c, l/B	$h = B/8$	$B/12$	$B/16$	$B/24$	$B/32$	Extrapolated
l/h for l/B = 0.1 (0.05)	0.8 (0.4)	1.2 (0.6)	1.6 (0.8)	2.4 (1.2)	3.2 (1.6)	
Q4, c = 2, l/B = 0.1	>1680 [a]	1406	1255	1153	1109	–
Q8R, c = 2, l/B = 0.1	>1266 [a]	1208	1173	–	–	–
Q8R, c = 0.5, l/B = 0.1	1056	985	953	–	–	–
Q8R, c = 0.5, l/B = 0.05	976	921	890	859	–	≈800
s/B at the peak	0.149	0.163	0.158	0.156	–	
D at s/B = 10%/20%	20.5/64.3	20.9/61.2	19.9/59.7	–	–	
band thickness (m)	0.42	0.38	0.39	–	–	

[a] at s/B = 20%, no peak.

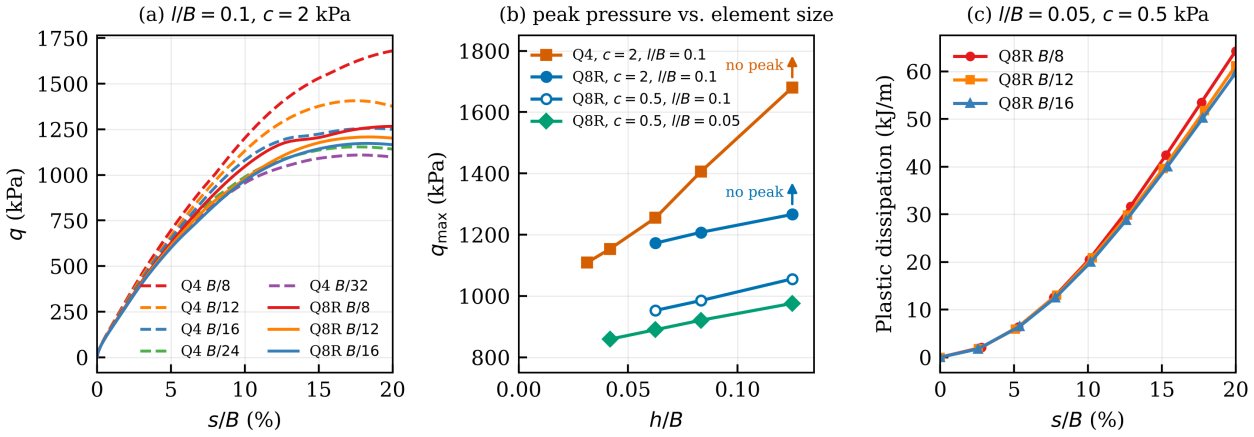

Figure 5. Mesh convergence at fixed internal length: (**a**) load–settlement curves for l/B = 0.1, c = 2 kPa, Q4 and Q8R elements; (**b**) peak pressure versus element size (arrows: no peak by s/B = 20%); (**c**) plastic dissipation versus settlement for l/B = 0.05, c = 0.5 kPa.

5.4. Load–Settlement Response and Internal Length

Figure 6 shows the load–settlement curves of the Q8R analyses on the $B/16$ mesh with c = 0.5 kPa, and Table 7 gives the peak values. All Cosserat analyses reach a clear peak at s/B = 15–16%, followed by softening. The peak pressure increases with the internal length: 834, 890 and 953 kPa for l/B = 0.025, 0.05 and 0.1, i.e., by about 7% per doubling of l/B, while the initial response is almost independent of l. With c = 2 kPa the corresponding values are 1005, 1078 and 1173 kPa, i.e., a cohesion term of about 125 kPa per kPa (Section 5.5). With the Q4 element, the dependence of the peak on l/B appears weaker (1189–1255 kPa), because the overestimate of the capacity by this stiffer element masks part of the effect of l.

5.5. Influence of the Numerical Cohesion

The cohesion needed for numerical stability adds a term cN_c to the capacity, with $N_c \approx 102$ for φ_p, which is not negligible: c = 2 kPa corresponds to about 200 kPa. The reference analysis ($h = B/16$, Q4, l/B = 0.05) was therefore repeated with c = 1, 0.5 and 0.25 kPa (Table 8). With c = 0 the global iteration fails within the first increments, as explained in Section 5. The peak pressure decreases linearly with c, by 110 kPa per kPa of cohesion (least-squares fit of the three completed analyses). This value is close to N_c, i.e., the cohesion acts as the classical cohesion term and does not change the mechanism. The extrapolation to c = 0 gives $q_{max} \approx 1000$ kPa, 18% below the value for c = 2 kPa and 5% below the value for c = 0.5 kPa. The study was repeated with the Q8R element of the main analyses ($h = B/16$, l/B = 0.05), with which all analyses reached the peak: c = 2, 0.5 and 0.25 kPa give 1078, 890

and 850 kPa. The slope is 125 kPa per kPa between 2 and 0.5 kPa and increases to 157 kPa per kPa between 0.5 and 0.25 kPa, so a linear extrapolation from the two smallest values, $q_{\max} \approx 810$ kPa for $c \to 0$, is an upper estimate. The main analyses use $c = 0.5$ kPa. Their capacities exceed the cohesionless values by about 40–55 kPa (5–6%), and this correction is applied where the results are compared with solutions for $c = 0$.

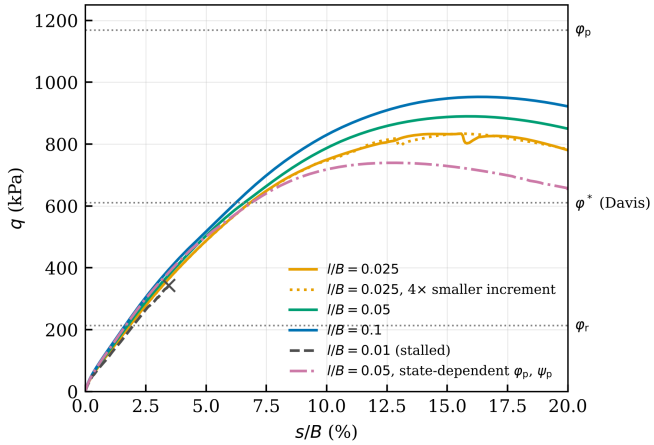

Figure 6. Load–settlement curves (Q8R, $h = B/16$, $c = 0.5$ kPa) for different internal lengths and for stress- and density-dependent peak angles. Horizontal lines: rigid–plastic collapse pressure ($cN_c + \frac{1}{2}\gamma BN_\gamma$, exact N_γ [5]) for φ_p, Davis' reduced angle φ^* and φ_r. The short temporary drops (3–4%) of the $l/B = 0.025$ curves are local events in the poorly resolved band ($l/h = 0.4$): their position changes with the load increment ($s/B = 15.6\%$ with the standard increment, 12.9% with a four times smaller one), whereas the peak (834 kPa at $s/B = 15.6\%$) and the rest of the curve are unchanged. The cross marks the end of the near-classical analysis ($l/B = 0.01$), which stalls before the peak.

Table 7. Peak pressure and settlement at the peak (Q8R, $h = B/16$, $B = 1$ m).

l/B	l/h	$q_{\max}$ (kPa), $c = 0.5$	s/B at peak	$q_{\max}$ (kPa), $c = 2$
0.01	0.16	>343 [a]	–	–
0.025	0.4	834	0.156	1005
0.05	0.8	890	0.158	1078
0.1	1.6	953	0.162	1173
0.05, state-dependent φ_p, ψ_p	0.8	739	0.129	–

[a] stalled at $s/B = 3.5\%$.

Table 8. Influence of the numerical cohesion ($h = B/16$, $l/B = 0.05$): peak pressure and settlement at the peak for Q4 and Q8R elements.

c (kPa)	2	1	0.5	0.25	0 (Extrapolated)
Q4: $q_{\max}$ (kPa)	1219	1103	1056 [a]	≥996 [b]	≈1000
s/B at the peak	0.175	0.161	0.155	–	–
Q8R: $q_{\max}$ (kPa)	1078	–	890	850	≲810
s/B at the peak	0.175	–	0.158	0.153	–

[a] the analysis stopped at the peak ($s/B = 0.155$) with repeated step reductions; [b] stopped at $s/B = 0.127$, before the peak.

5.6. Comparison with Bearing Capacity Solutions

Classical bearing capacity solutions assume a rigid–perfectly plastic material with a single friction angle. They cannot validate a model with hardening, softening and non-associated flow, but they serve here as references that bracket the computed capac-

ity and indicate which strength is mobilised at failure. Table 9 gives the superposition $q_u = cN_c + \frac{1}{2}\gamma BN_\gamma$ with $c = 0.5$ kPa, $N_q = e^{\pi \tan\varphi}\tan^2(45° + \varphi/2)$, $N_c = (N_q - 1)\cot\varphi$ and five expressions for N_γ: Meyerhof [3], Hansen [64], Eurocode 7 [65], Vesić [4], and the exact value for a rough base of Martin [5], interpolated log-linearly between his tabulated values. Three friction angles are used: the peak angle $\varphi_p = 42.75°$; Davis' reduced angle for non-associated flow, $\tan\varphi^* = \cos\psi\sin\varphi/(1 - \sin\psi\sin\varphi)$, which gives $\varphi^* = 39.4°$ for $\psi_p = 18.6°$; and the residual angle $\varphi_r = 33.3°$.

Table 9. Bearing capacity of the rough strip footing ($B = 1$ m, $\gamma = 15$ kN/m^3, $c = 0.5$ kPa): analytical solutions and finite element peak pressures (kPa).

Solution	$\boldsymbol{\varphi_p = 42.75°}$	$\boldsymbol{\varphi^* = 39.4°}$	$\boldsymbol{\varphi_r = 33.3°}$
Meyerhof [3]	1270	661	227
Hansen [64]	1033	572	212
Eurocode 7 [65]	1360	751	276
Vesić [4]	1387	776	296
Exact, rough base [5]	1168	611	214
Finite element (Q8R)	$\boldsymbol{l/B = 0.025}$	$\boldsymbol{l/B = 0.05}$	$\boldsymbol{l/B = 0.1}$
Constant peak angles, $h = B/16$	834	890	953
Constant peak angles, $h \to 0$ (extrapolated)	–	≈800 [a]	–
State-dependent peak angles, $h = B/16$	–	739	–
State-dependent peak angles, $h = B/24$	–	716	–

[a] ≈745 kPa for $c \to 0$.

The mesh-converged Cosserat capacity (≈800 kPa for $l/B = 0.05$) lies between the rigid–plastic values for Davis' reduced angle (611 kPa) and for the peak angle (1168 kPa): about 30% above the former and 30% below the latter. Q4 analyses with $c = 2$ kPa give peak pressures within 10% of the associated solution with φ_p. The benchmarks and the mesh study show that this agreement is fortuitous: it results from the overestimate of the Q4 element and from the cohesion of 2 kPa. The Q8R results are consistent with what is expected for a dilatant sand that softens after the peak. The peak strength is not mobilised simultaneously along the whole slip surface (Section 5.9), and the non-associated flow reduces the capacity, although by less than Davis' reduction suggests, as also found by Loukidis and Salgado [7]. The two effects were separated by perfectly plastic analyses with the peak angles and without hardening or softening, on the same mesh (Q8R, $h = B/16$, $c = 0.5$ kPa). With $l/B = 0.05$, the associated material ($\varphi = \psi = 42.75°$) gives 1917, 1973 and 1991 kPa at $s/B = 10$, 15.8 and 20%, and the non-associated material ($\varphi = 42.75°$, $\psi = 18.6°$) 1629, 1696 and 1717 kPa; both are still rising slowly at $s/B = 20\%$. The softening model gives 787 and 890 kPa (peak) at $s/B = 10$ and 15.8%. Near the classical limit ($l/B = 0.005$), the associated analysis reaches a practically constant pressure of 1406 kPa, 20% above the exact value of 1168 kPa on this mesh, and the non-associated analysis gives 1062 kPa at $s/B = 4\%$, 12% below the associated one at the same settlement, before it stalls when a narrow band forms. At equal settlement, the non-associated flow therefore reduces the pressure by 12–14%, much less than the 48% implied by Davis' reduced angle, while hardening, softening and the progressive mobilisation of the peak strength reduce it by a further 48% (1696 to 890 kPa at $s/B = 15.8\%$). Within this model, the gap between the computed capacity and the rigid–plastic solution for φ_p is thus caused mainly by progressive failure and only secondarily by the non-associated flow. The analyses also show that, in the perfectly plastic material, the internal length $l/B = 0.05$ raises the pressure by about 40% (1404 to 1973 kPa at $s/B = 15.8\%$), much more than in the softening material (about 7% per doubling of l/B, Section 5.4), consistent with the N_γ benchmark (Section 5.2). Values

computed with φ_r (210–300 kPa) are a lower bound for the fully softened soil and are far below the computed peak. Among the design formulae, Hansen's expression with φ^* is the most conservative and is about 30% below the computed capacity. All expressions evaluated with φ_p overestimate the capacity of the softening sand by 30–70%.

5.7. Failure Mechanism and Wedge Angle

The wedge angle α under the footing was measured from the incremental displacement field between two states; in the rigid wedge, the velocity is vertical. In each column of nodes under the footing, the depth at which the velocity first deviates from the vertical by more than 10° was found, and a line through the footing edge was fitted to these points. Figure 7 shows the result for the Q8R analyses ($h = B/16$, $c = 0.5$ kPa) over the settlement interval that follows the peak. For $l/B = 0.025$, 0.05 and 0.1, the wedge angle is $\alpha_d = 65°$, 65° and 67°, and 63° with the state-dependent peak angles. Evaluated over the whole range from $s/B = 10\%$ to 20%, the constant-angle analyses give $\alpha_d = 58$–67° and the state-dependent analysis 55–63°, with the smaller values late in the post-peak range. These values are close to the Prandtl value $45° + \varphi_p/2 = 66.4°$ and much steeper than Terzaghi's assumption $\alpha = \varphi$. As softening spreads after the peak, they decrease towards $45° + \varphi_r/2 = 61.7°$ for the residual friction angle. The internal length has only a small effect on α in the range studied. Its main effect is on the shear zone at the footing edge, which is wider and more diffuse for larger l/B (Section 5.4). An analysis close to the classical limit ($l/B = 0.01$) could not be continued to the peak on this mesh (Section 5.3), so that no classical mechanism can be shown.

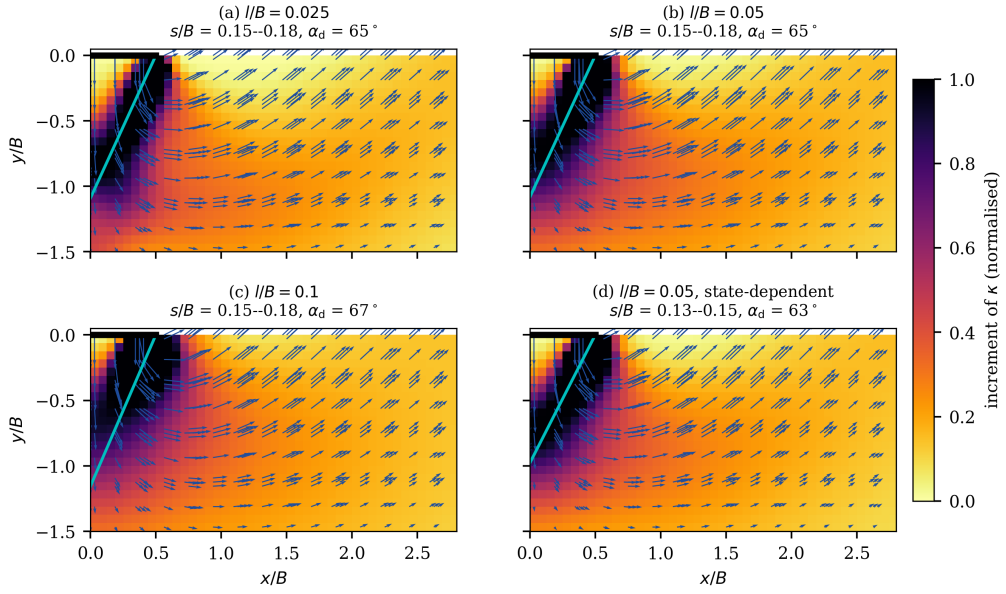

Figure 7. Failure mechanism just after the peak (Q8R, $h = B/16$, $c = 0.5$ kPa): increment of κ over the settlement interval indicated (normalised) and incremental displacement vectors (arrows) for (**a**–**c**) constant peak angles with $l/B = 0.025$, 0.05 and 0.1 and (**d**) stress- and density-dependent peak angles with $l/B = 0.05$. The line is the boundary of the rigid wedge from the velocity criterion; α_d is its angle to the horizontal.

5.8. Comparison of the Computed Mechanism with Analytical Mechanisms

Figure 8 compares the computed fields of the Q8R analysis with $l/B = 0.05$ ($h = B/16$, $l/h = 0.8$, $c = 0.5$ kPa) with the Prandtl mechanism for the peak, the Davis-reduced and the residual friction angles, and with Terzaghi's wedge ($\alpha = \varphi_p$). The incremental fields are taken over $s/B = 15.4$–17.8%, i.e., just after the peak ($s/B = 15.6\%$). The rigid

wedge under the footing (Figure 8c) is bounded by lines at about 65°, close to the Prandtl wedge for φ_p (66.4°) and much steeper than Terzaghi's wedge. The zone of significant incremental displacement ($|\Delta u|/|\Delta s| > 0.3$) reaches the surface at $x \approx 3.9B$ and a depth of about $1.6B$; the zone with $|\Delta u|/|\Delta s| > 0.1$ reaches $x \approx 5.1B$ and a depth of $2.3B$. This is much smaller than the Prandtl mechanism of the peak angle (surface exit at $10.3B$, depth $2.7B$) and of the Davis angle ($8.2B$, $2.3B$), and comparable to that of the residual angle ($5.7B$, $1.8B$). The accumulated plastic variable (Figure 8a) is largest along the side of the wedge and in the radial zone next to the footing edge, where the soil has softened, while the material further out has remained near the peak (Section 5.9). The Cosserat rotation (Figure 8d) is concentrated in the same zone at the footing edge, with a maximum of about 28°; elsewhere it is small, so the micropolar terms act only where the deformation localises. At failure, the mechanism in the dense sand is therefore a contracted Prandtl mechanism: the wedge is close to that of the peak angle, while the extent of the mechanism is controlled by the softened soil, and the peak pressure (Table 9) by the peak strength mobilised before softening spreads.

5.9. Progressive Failure

Figure 9 shows the development of the accumulated plastic variable κ and of the friction and dilatancy angles that it implies, $\varphi(\kappa)$ and $\psi(\kappa)$ (Equation (12)), at $s/B = 5$, 10, 15 (peak) and 20% for $l/B = 0.05$. At $s/B = 5\%$, the peak friction angle is reached only in a zone below the footing edge, and most of the future mechanism is still in the hardening branch, with $\varphi = 31$–$38°$ and contractant or weakly dilatant behaviour. At $s/B = 10\%$, the peak angle is mobilised in a large zone that extends from below the footing towards the passive side. Softening has started at the footing edge, where κ exceeds κ_p and φ and ψ decrease. At the peak ($s/B = 15\%$), the zone at peak strength extends to about $1.5B$ from the axis, while the soil close to the free surface on the passive side is still hardening ($\varphi \approx 36$–$39°$). At the same time a softened band ($\varphi < 36°$, $\psi < 5°$) has formed from the footing edge along the boundary of the wedge, and the material under the centre of the footing has started to soften. After the peak ($s/B = 20\%$), the softened band extends along the wedge boundary, while the outer part of the mechanism is still at or near the peak.

The peak pressure thus corresponds to a state in which the peak strength is mobilised over most, but not all, of the slip surface. At the footing edge, where the strains are largest, the strength has already dropped towards the residual value, while at the end of the passive zone the soil has not yet reached the peak. This progressive mobilisation explains why the computed capacity lies between the rigid–plastic solutions for φ_p and for the reduced angles (Table 9). It also explains why the peak pressure depends on the internal length: a larger l widens the softening band at the edge and delays its propagation.

5.10. Stress- and Density-Dependent Peak Angles

In the analyses above, the peak angles are those of TMD22. In the footing, however, the mean stress varies from almost zero at the surface to several hundred kPa below the footing, and the sand loosens where it dilates. To examine the effect of these changes, the analysis with $l/B = 0.05$ was repeated with peak angles that depend on the current state of each Gauss point. Bolton's relation (Equation (14)) is evaluated with the current mean stress p and the current void ratio $e = e_0 + (1 + e_0)\varepsilon_v$, at the start of each increment, with the constants fitted to the five triaxial tests ($A = 1.48$, $Q = 13.70$, $R = 1$; Section 4) and $0 \le I_R \le 8$. The dilatancy angle is set to zero when e reaches the critical void ratio $e_c(p) = e_{c0}\exp[-(3p/h_s)^n]$ with the hypoplastic parameters of the sand ($e_{c0} = 1.054$, $h_s = 355$ MPa, $n = 0.27$), with a linear transition over $\Delta e = 0.01$. This variant reproduces the peaks of TMD21–TMD25 within −3% to +4% (Table 3, column (iii)).

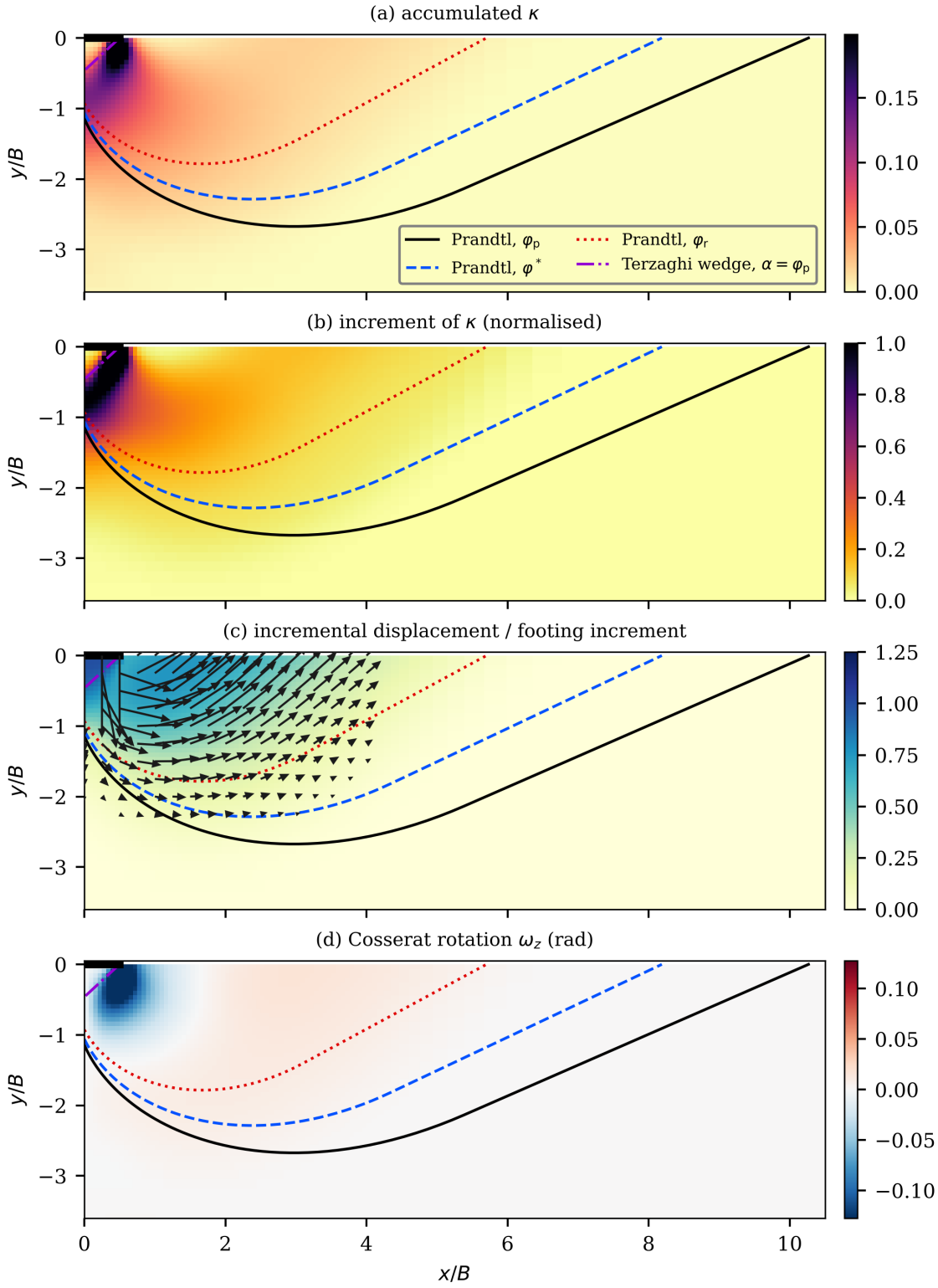

Figure 8. Computed fields for $l/B = 0.05$ (Q8R, $h = B/16$, $c = 0.5$ kPa; accumulated values at $s/B = 17.8\%$, increments over $s/B = 15.4$–17.8%) with analytical failure mechanisms superimposed: (**a**) accumulated plastic variable; (**b**) increment of κ (normalised); (**c**) incremental displacement magnitude and vectors (arrows), normalised by the footing increment; (**d**) Cosserat rotation. Lines: Prandtl mechanism for φ_p, φ^* and φ_r, and Terzaghi's wedge with $\alpha = \varphi_p$.

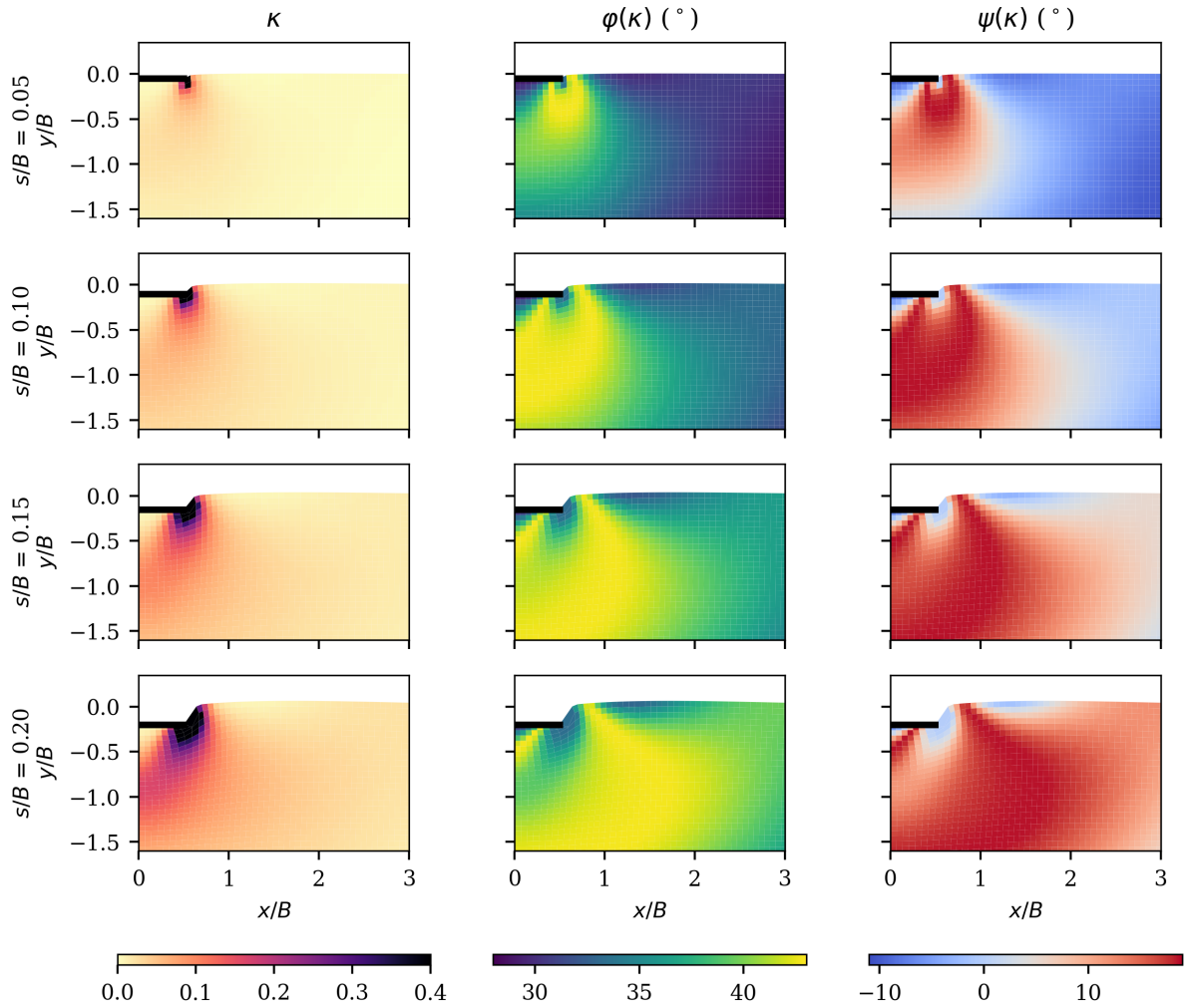

Figure 9. Progressive failure for $l/B = 0.05$ (Q8R, $h = B/16$, $c = 0.5$ kPa), shown on the deformed mesh: accumulated plastic variable κ and the mobilised friction and dilatancy angles $\varphi(\kappa)$ and $\psi(\kappa)$ at $s/B = 5$, 10, 15 (peak) and 20%. Black line: footing.

The stress- and density-dependent analysis gives a peak pressure of 739 kPa at $s/B = 12.9\%$, 17% below the analysis with constant angles, followed by a stronger softening (Figure 6). Close to the surface, where p is small, the peak friction angle is higher than in TMD22. Beneath the footing, however, the mean stress reaches 300–600 kPa and φ_p is 1–2° lower. In addition, the dilation loosens the sand, so that I_R and ψ decrease during shearing and ψ vanishes when the critical void ratio is approached. The second effect is not contained in the constant-angle model, which keeps $\psi_p = 18.6°$ regardless of the accumulated dilation. The wedge angle ($\alpha_d = 55$–$63°$) and the extent of the mechanism are similar in both analyses. The comparison does not depend on the mesh: on the finer mesh ($h = B/24$) the state-dependent analysis gives 715.7 kPa at $s/B = 12.5\%$, 3.2% below the $B/16$ value, which is the same mesh correction as for constant angles (858.8 against 889.7 kPa, −3.5%). The ratio of the two capacities is 0.831 on $B/16$ and 0.833 on $B/24$, and the extrapolated capacities are about 670 and 800 kPa. The constant-angle analyses therefore overestimate the capacity by about 15–20% at this footing width, and the stress- and density-dependent variant is preferable for quantitative predictions. Its effect on the scale effect is shown in Section 5.11.

5.11. Scale Effect

The scale effect was studied with the Q8R element for $B = 0.5$, 1, 2 and 4 m. Geometry, mesh ($h = B/16$), settlement steps, internal length ($l/B = 0.05$) and cohesion ($c = 0.5B$ kPa) were scaled with B, so that l/B and $c/(\gamma B)$ are the same for all widths. With constant strength parameters, a rigid–plastic solution then gives the same $N_\gamma^* = 2q/(\gamma B)$ for every B; the cohesion contributes the same amount, about $2cN_c/(\gamma B) \approx 7$, to all of them. Any remaining dependence on B must therefore come from the stiffness, which increases only with the square root of the stress level (Equation (4)), or, in the analyses with state-dependent peak angles (Section 5.10), from the decrease in the peak angles with the stress level. To separate the two, the analyses with $B = 4$ m were repeated with the Young's modulus multiplied by $2 = \sqrt{4}$, which gives the same ratio $E/(\gamma B)$ as for $B = 1$ m. The effect of the internal length is given by the analyses with $B = 1$ m and $l/B = 0.025$, 0.05 and 0.1 (Section 5.4). All analyses were carried beyond the peak to $s/B = 20\%$ (Figure 10, Table 10), so no lower bounds are involved.

Table 10. Scale effect (Q8R, $h = B/16$, $l/B = 0.05$, $c = 0.5B$ kPa): normalised pressure $N_\gamma^* = 2q/(\gamma B)$ at $s/B = 10\%$ and at the peak, and settlement at the peak. $E \times 2$: Young's modulus doubled, so that $E/(\gamma B)$ is the same as for $B = 1$ m.

	$B = 0.5$ m	$B = 1$ m	$B = 2$ m	$B = 4$ m	$B = 4$ m, $E \times 2$
Constant peak angles					
N_γ^* at $s/B = 10\%$	110.7	104.9	95.8	84.4	103.1
N_γ^* at peak	121.1	118.6	115.4	112.1	117.7
s/B at peak (%)	15.3	15.8	17.0	18.7	16.0
State-dependent peak angles					
N_γ^* at $s/B = 10\%$	105.0	95.7	85.5	74.4	81.3
N_γ^* at peak	106.7	98.6	90.6	82.9	83.1
s/B at peak (%)	12.1	12.9	13.6	14.9	11.9

With constant peak angles, the peak value of N_γ^* decreases only slightly, by about 2.5% per doubling of B, from 121.1 to 112.1 between $B = 0.5$ and 4 m, and the peak moves to larger settlements (15.3% to 18.7%). The decrease at $s/B = 10\%$ is larger (110.7 to 84.4), because a larger footing is relatively softer and mobilises a smaller part of its strength at a given s/B. The analysis with $E \times 2$ confirms that this is a stiffness effect: with the same $E/(\gamma B)$ as for $B = 1$ m, the $B = 4$ m footing gives $N_\gamma^* = 117.7$ at the peak (118.6 for $B = 1$ m), 103.1 at $s/B = 10\%$ (104.9) and a peak at $s/B = 16.0\%$ (15.8%). About 85% of the scale effect at the peak, and practically all of it before the peak, is therefore explained by the stress-dependent stiffness. Because l/B is constant in this series, the internal length does not contribute. Its effect at fixed B is of a similar size: for $B = 1$ m, N_γ^* at the peak is 111.2, 118.6 and 127.1 for $l/B = 0.025$, 0.05 and 0.1, i.e., about 7% per doubling of l/B. If l were a material constant, l/B would halve with each doubling of B, and this would add a decrease of about 7% per doubling to the stiffness effect. Since l is used here as a regularisation parameter (Section 7), this Cosserat part of the scale effect cannot be quantified for real footings without a physically identified l.

With state-dependent peak angles, the scale effect is much stronger: the peak value decreases by 7–8% per doubling of B, from 106.7 to 82.9, and the peak settlement increases from 12.1% to 14.9%. Doubling the stiffness of the $B = 4$ m footing leaves the peak practically unchanged (83.1 against 82.9) and only moves it to a smaller settlement. In this case, the scale effect is caused by the decrease in the mobilised peak angles with the stress level, i.e., by the classical mechanism of the curvature of the strength envelope of dense sand [15]. Compared with the constant-angle analyses, the state-dependent peak angles reduce the capacity by

12% for $B = 0.5$ m and by 26% for $B = 4$ m. Within the present model, the scale effect at the peak therefore comes mainly from the stress dependence of the strength, secondarily from the stiffness, and from the internal length only if l/B changes with B.

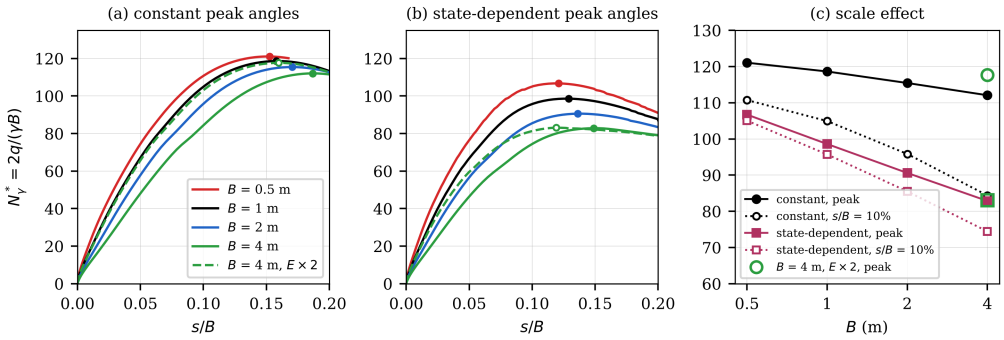

Figure 10. Scale effect (Q8R, $h = B/16$, $l/B = 0.05$, $c = 0.5B$ kPa): normalised pressure $N_\gamma^* = 2q/(\gamma B)$ versus s/B for (**a**) constant and (**b**) state-dependent peak angles (dots: peaks; dashed: $B = 4$ m with the Young's modulus doubled); (**c**) N_γ^* at the peak and at $s/B = 10\%$ versus footing width (open green symbols: $B = 4$ m with $E \times 2$).

6. Second Example: Footing at the Crest of a Slope, Comparison with a Classical Code

The footing analyses of Section 5 show that the Cosserat solution converges with mesh refinement, but a classical analysis of the same problem could not be carried to the peak (Section 5.3). To show directly what the Cosserat terms change, a second example was analysed with the present code and with a commercial classical finite element code (ANSYS Mechanical APDL 2024 R2, Mohr–Coulomb model `TB,MC`) on identical meshes. The problem is a rigid footing at the crest of a cohesive-frictional slope, a configuration in which a single inclined shear band forms from the footing to the toe [28].

6.1. Model

The slope is 10 m high and inclined at 45°, with a base of 20 m and a crest of 10 m (Figure 11). A rigid footing, 4 m wide and 1 m thick, rests on the crest at its edge; it is modelled with stiff, weightless elastic elements that share the nodes of the soil surface (bonded interface). The base is fixed and the right boundary is restrained horizontally. After the gravity step, a vertical displacement U is prescribed only at the middle node of the footing top, so that the footing can rotate and move horizontally with the soil. The soil is a Mohr–Coulomb material with $E = 10$ MPa, $\nu = 0.40$, $\gamma = 20$ kN/m^3, $\varphi = 10°$, $\psi = 3.7°$ and $c_0 = 40$ kPa, without a tension cut-off. Two cases are considered: (A) perfect plasticity, and (B) linear softening of the cohesion with the hardening variable, from 40 kPa to 28 kPa at $\kappa = 0.12$ (softening modulus -100 kPa), constant afterwards. The residual cohesion was chosen so that the slope remains stable under its self-weight after softening; with a lower residual value, the slope fails under gravity once the band has formed, and the footing force becomes negative.

Three structured meshes with 10×10, 20×20 and 40×40 eight-node quadrilaterals in the soil and 4×1, 8×2 and 16×4 in the footing were generated in ANSYS (PLANE183, plane strain) and imported unchanged into the Cosserat code (Q8R). In the Cosserat analyses, $a = 0.56$ and two internal lengths were used: $l = 0.01$ m, which is small compared with all element sizes ($l/h \leq 0.04$) and gives an essentially classical response, and $l = 0.141$ m ($l/h = 0.14$–0.56 for the three meshes). ANSYS was run with its elastic tangent for the

Mohr–Coulomb model, as recommended for this model, and the Cosserat code with the consistent tangent; the converged solutions do not depend on this choice.

The two codes were first compared on a single element in plane-strain compression under a confining pressure of 50 kPa (Appendix A, Figure A1). For perfect plasticity, both give the same strength, 166.354 kPa. The hardening variable that governs the cohesion scaling function of ANSYS was back-calculated from its stress–strain curve; it equals 0.865 times the ANSYS equivalent plastic strain and agrees with the accumulated plastic multiplier κ of the present model within 2%. The same softening table was therefore used in both codes, and the softening responses agree within 0.1% up to 4% axial strain.

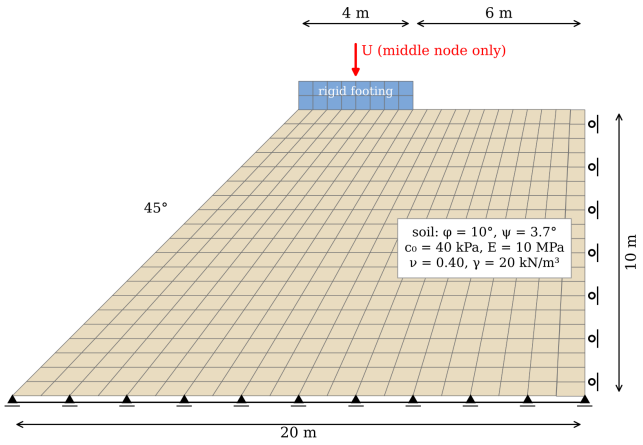

Figure 11. Slope with a rigid footing at the crest: geometry, boundary conditions, soil parameters and the 20×20 mesh. The vertical displacement U is prescribed only at the middle node of the footing top. Triangles: fixed base ($u_x = u_y = 0$); circles: rollers on the right boundary ($u_x = 0$).

6.2. Case A: Perfect Plasticity

Figure 12 and Table 11 show the load–settlement curves. With $l = 0.01$ m, the Cosserat code reproduces the ANSYS results on all three meshes: the limit force differs by 0.5–3% (at $U = 500$ mm, 586, 549 and 534 kN/m against 569, 542 and 527 kN/m), the initial stiffness is the same, and the footing rotates clockwise by 1–2.5° in both codes. This is a direct verification of the implementation against an independent code on a boundary value problem with non-associated flow and a rotating footing. In both classical analyses, the limit force converges with mesh refinement, as expected without softening, but the shear band from the right footing edge to the toe always spans one to two elements and the plastic strain in it increases with refinement (at $U = 500$ mm, 0.23, 0.37 and 0.55 in ANSYS). With $l = 0.141$ m, the band has a finite width of about 1–1.5 m on the two finer meshes, the maximum of κ (0.22–0.26) no longer increases with refinement, and the couple stresses in the band raise the limit force by 15–17%.

Table 11. Slope with a crest footing: footing force F (kN/m) at the peak and at two settlements on the different meshes.

Model	Mesh	Case A (Perfect Plasticity)			Case B (Softening)		
		Peak	$U = 100$ mm	$U = 500$ mm	Peak	$U = 100$ mm	$U = 500$ mm
ANSYS (classical)	10×10	571	559	569	546	453	256
	20×20	556	535	542	521	303	217
	40×40	555	534	527	502	234	204
	80×80	–	–	–	505 [a]	209 [a]	197 [a]

Table 11. *Cont.*

Model	Mesh	Case A (Perfect Plasticity) Peak	$U = 100$ mm	$U = 500$ mm	Case B (Softening) Peak	$U = 100$ mm	$U = 500$ mm
Cosserat, $l = 0.01$ m	10 × 10	586	573	586	543	493	263
	20 × 20	549	546	549	512	378	224
	40 × 40	534	532	534	486	259	209
	80 × 80	–	–	–	454	– [b]	– [b]
Cosserat, $l = 0.141$ m	10 × 10	658	636	658	606	596	338
	20 × 20	642	621	642	589	581	335
	40 × 40	632	612	632	580	574	333
	80 × 80	–	–	–	576	573	331

[a] with numerical stabilisation (stabilisation energy 0.8% of the strain energy); without it, peak 501.5 kN/m and no convergence beyond $U = 67$ mm. [b] no convergence beyond $U = 62$ mm. The 80 × 80 mesh was analysed for case B only.

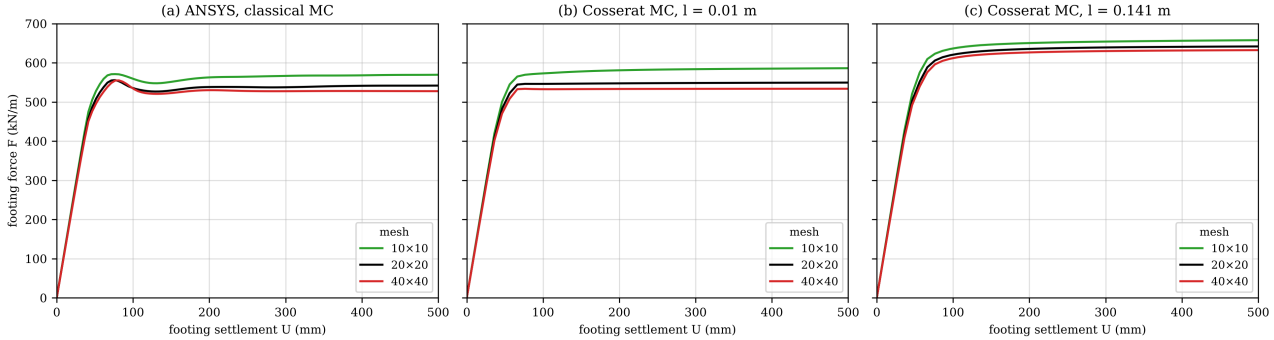

Figure 12. Slope, case A (perfect plasticity): footing force versus settlement on the three meshes for (**a**) ANSYS, (**b**) the Cosserat code with $l = 0.01$ m and (**c**) with $l = 0.141$ m.

6.3. Case B: Softening

With softening, the classical response becomes mesh-dependent (Figure 13, Table 11). In ANSYS, the peak force decreases from 546 to 521 and 502 kN/m from the 10 × 10 to the 40 × 40 mesh, and the finer the mesh, the earlier and faster the post-peak branch drops: at $U = 100$ mm the force is 453, 303 and 234 kN/m. The shear band always spans about two elements: its width w, measured as the full width at half maximum of the plastic strain on horizontal sections at $y = 3$, 5 and 7 m, is 3.09, 1.62, 0.80 and 0.43 m at $U = 500$ mm on the 10 × 10 to 80 × 80 meshes, i.e., it halves with the element size. The equivalent plastic strain in the band increases with refinement, from 0.35 to 0.55 and 0.85 at $U = 500$ mm (Figure 14). On the finest mesh, the formation of the narrow band produces an abrupt drop of the force at $U \approx 68$ mm. The Cosserat code with $l = 0.01$ m shows the same behaviour (peaks 543, 512 and 486 kN/m; 493, 378 and 259 kN/m at $U = 100$ mm), which shows that the mesh dependence is a property of the classical continuum and not of either code. On an additional 80 × 80 mesh, ANSYS reaches the peak (501.5 kN/m at $U = 64$ mm) but fails to converge at $U = 67$ mm, when the narrow band forms and the force drops abruptly; the minimum load increment is reached and the analysis stops. The analysis could be completed only with a small energy-based numerical stabilisation (the dissipated stabilisation energy is 0.8% of the strain energy at the end): peak 505 kN/m, 209 kN/m at $U = 100$ mm and 197 kN/m at 500 mm, i.e., the post-peak force decreases further with refinement. The Cosserat code with $l = 0.01$ m behaves in the same way on this mesh: the peak decreases further, to 454 kN/m, and the analysis cannot be continued beyond $U = 62$ mm, shortly after the peak.

With $l = 0.141$ m, the load–settlement curves of the 20 × 20, 40 × 40 and 80 × 80 meshes coincide over the whole range: peak 589, 580 and 576 kN/m, 581, 574 and 573 kN/m at $U = 100$ mm, 494, 491 and 493 kN/m at 200 mm and 335, 333 and 331 kN/m at 500 mm (differences of 0.5–1.5%, and below 1% between the two finest meshes, on which $l/h = 0.56$

and 1.13); the coarse mesh, on which the internal length is not resolved ($l/h = 0.14$), is 2–3% higher. The softening is gradual and reflects the progressive formation of the band rather than the element size. The band width converges with refinement: $w = 2.80$, 2.19, 2.06 and 2.02 m on the four meshes, i.e., about $15l$, whereas with $l = 0.01$ m it decreases in proportion to the element size, as in ANSYS (2.00, 1.25 and 0.60 m). The maximum of κ at $U = 500$ mm (0.32, 0.27 and 0.33) does not increase with refinement (Figure 15); the band widths are compared in Figure 16. On the 80 × 80 mesh, where ANSYS could not pass the peak without stabilisation, the Cosserat analysis reached $U = 500$ mm in 21 min without a single reduction in the load increment, with two to five Newton iterations per increment. The mechanism—a band from the right edge of the footing that curves through the slope to the toe, and a secondary, inactive band from the left footing edge—is the same as in the classical analyses. The internal length thus leaves the mechanism unchanged, but makes the band width, the dissipated energy and the post-peak response independent of the mesh, provided that the mesh resolves l. The coarse mesh, on which $l/h = 0.14$, is at the limit of this condition.

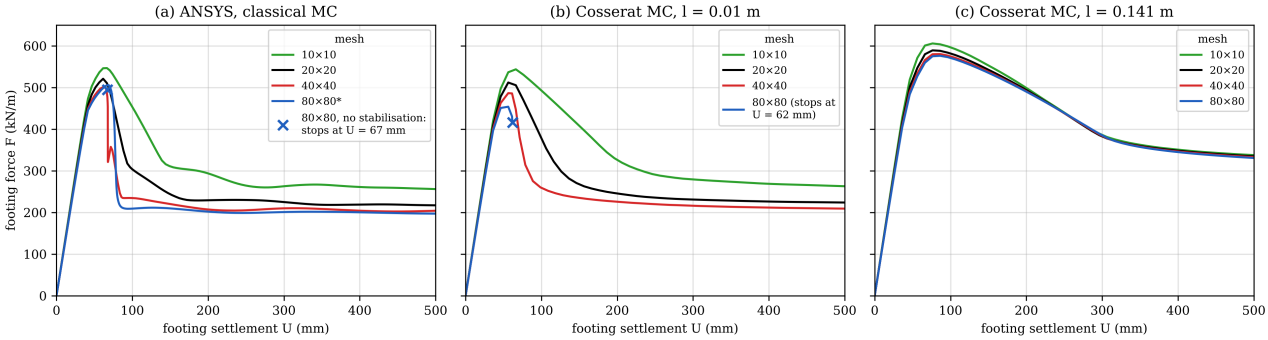

Figure 13. Slope, case B (softening): footing force versus settlement on the different meshes for (**a**) ANSYS, (**b**) the Cosserat code with $l = 0.01$ m and (**c**) with $l = 0.141$ m. In (**a**), the 80 × 80 curve (marked with an asterisk) was computed with numerical stabilisation; without it, the analysis stops at the cross. In (**b**), the 80 × 80 analysis stops at the cross.

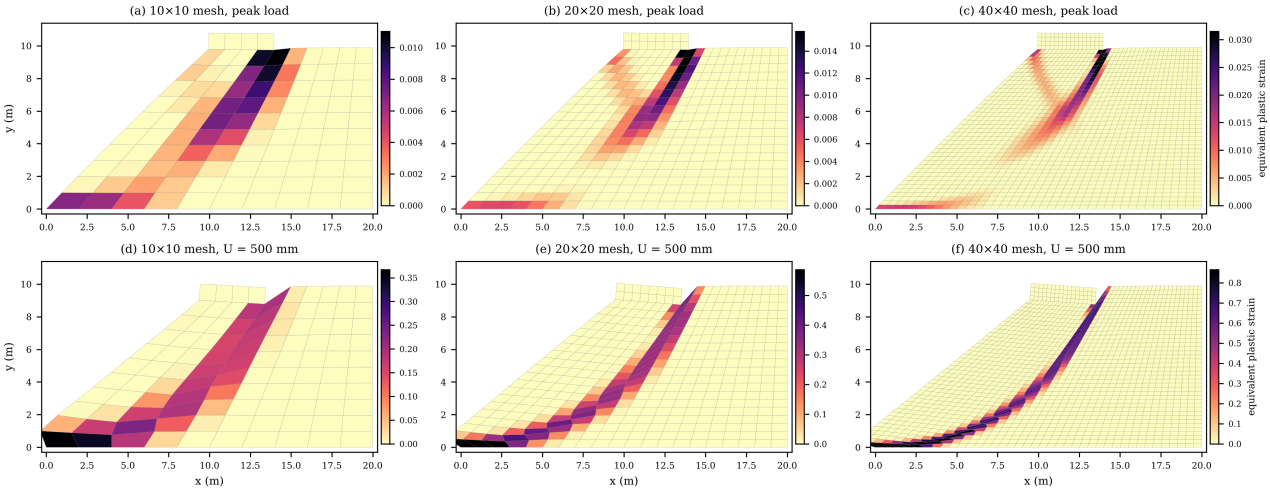

Figure 14. Slope, case B: equivalent plastic strain computed with ANSYS (classical Mohr–Coulomb) on the three meshes (**a**–**c**) at the peak force and (**d**–**f**) at $U = 500$ mm (deformation magnified twice).

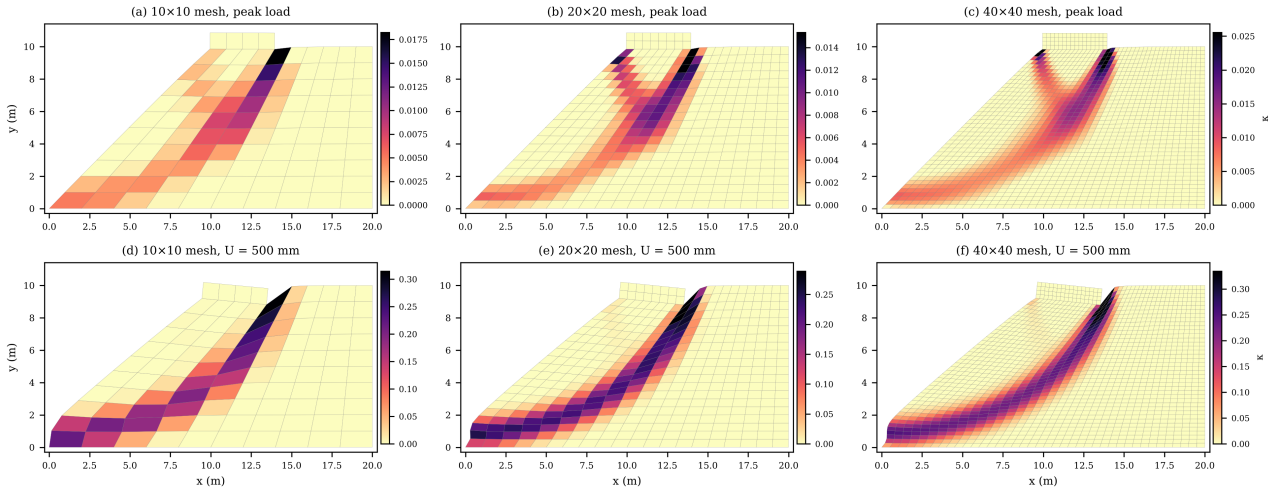

Figure 15. Slope, case B: accumulated plastic multiplier κ computed with the Cosserat model ($l = 0.141$ m) on the same meshes (**a**–**c**) at the peak force and (**d**–**f**) at $U = 500$ mm (deformation magnified twice).

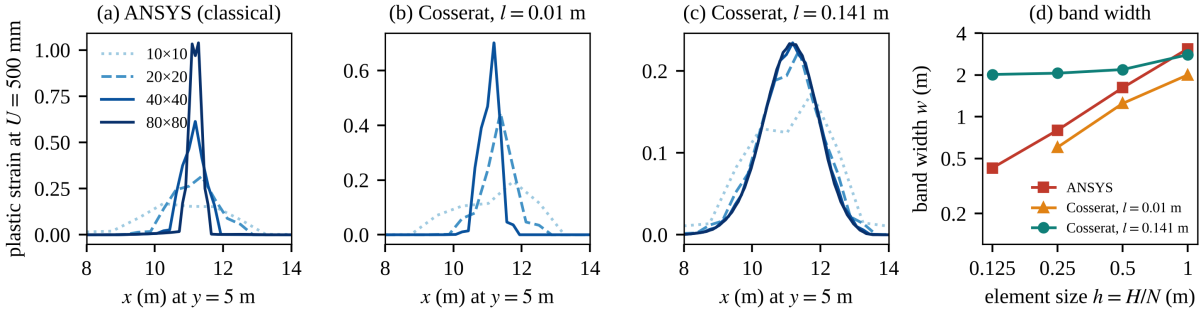

Figure 16. Slope, case B: width of the shear band at $U = 500$ mm. (**a**–**c**) Plastic strain (ANSYS: equivalent plastic strain; Cosserat: κ) along the horizontal section $y = 5$ m on the different meshes (80 × 80: ANSYS with numerical stabilisation; the Cosserat analysis with $l = 0.01$ m stopped at $U = 62$ mm on this mesh and is therefore not included in (**b**,**d**)); (**d**) band width w (full width at half maximum, mean of the sections $y = 3$, 5 and 7 m) versus element size $h = H/N$.

Sensitivity to the internal length. The internal length is a regularisation parameter (Section 7), and the slope response depends on it (Figure 17b, 40 × 40 mesh). The peak force increases from 534 to 561, 580, 605 and 643 kN/m for $l = 0.05$, 0.1, 0.141, 0.2 and 0.3 m, i.e., by about 5–11% per doubling of l, comparable to the footing (Section 5.4). The post-peak branch is more sensitive (258 to 462 kN/m at $U = 500$ mm), because l sets the width of the band and thus the volume that softens. On this mesh $l = 0.05$ m is not resolved ($l/h = 0.2$). As l decreases, the response approaches the classical one: with $l = 0.01$ m the peak is 486 kN/m and the force at $U = 500$ mm 209 kN/m, against 502 and 204 kN/m in ANSYS. The mesh independence shown above holds for a fixed l; a quantitative prediction of the post-peak response requires l to be identified physically.

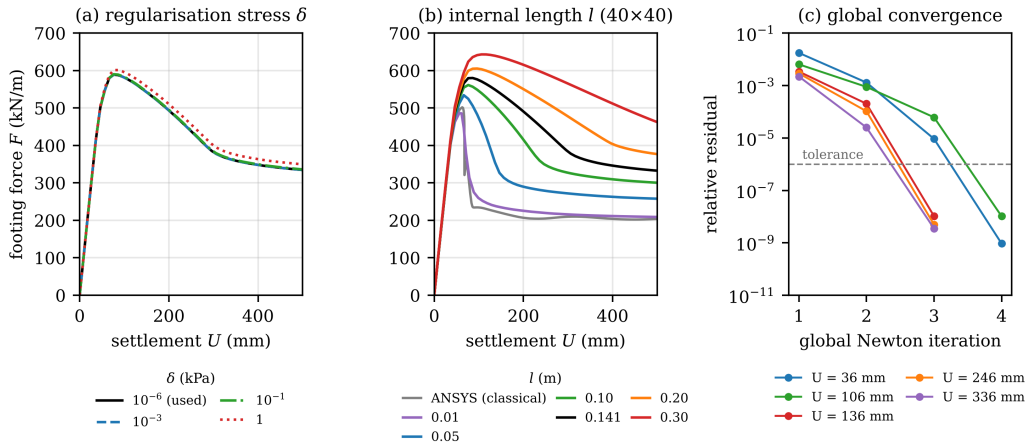

Figure 17. Slope, case B: (**a**) sensitivity to the regularisation stress δ of Equation (6) (20×20 mesh, $l = 0.141$ m); (**b**) sensitivity to the internal length l (40×40 mesh), with the classical ANSYS solution on the same mesh; (**c**) relative residual of the global Newton iteration in representative increments of analysis (**a**) with $\delta = 10^{-6}$ kPa.

7. Discussion

Calibration and its limits. The peak–residual laws reproduce the peak and residual strength and the dilatancy of the dense sand with seven parameters for the two angles. Over the complete curves of the five tests, the normalised error is 3–5% for the deviator stress and 0.2–0.9% strain for the volumetric strain between 50 and 300 kPa. The peak is reached at a smaller axial strain than in the tests (4.3% against 5.8–6.8%). Section 4 shows that this is a limitation of the two-parameter shape of the hardening branch rather than of the calibration; a third parameter, or a dependence of κ_p on the confining pressure, would be needed. Constant peak angles transfer reliably over 50–300 kPa. Bolton's relation predicts the peaks within about 5% in a leave-one-out test, with larger errors at the ends of the pressure range. The single internal variable κ synchronises the evolution of c, φ and ψ along proportional, monotonic paths from a normally consolidated state. The model therefore does not represent fabric, preshearing and sample preparation [61], monotonic preloading or drainage-dependent friction [62], non-coaxiality [43], or cyclic loading. It is intended for the first monotonic loading of a footing, for which the calibration tests are representative. Beneath the footing, the paths are monotonic but not proportional, and the principal axes rotate. The predictive capability of the model for such paths is therefore not established by the triaxial tests, which are proportional, and the progressive-failure results (Section 5.9) should be read with this limitation in mind.

Discretisation and verification. The verification (Section 3.3) and the benchmarks (Section 5.2) separate three sources of error in the footing analyses. The implementation itself reproduces exact solutions at the material point to round-off and converges to the exact collapse loads (within 2.5% for the cohesive problem, within 7% for N_γ once the Cosserat and cohesion terms are removed). The Q4 element with B-bar treatment locks in dilatant plastic flow and overestimates the capacity, as known for low-order elements [30,31]. This is the main reason for the high capacities of the Q4 analyses and for their strong mesh dependence between $h = B/8$ and $B/16$. With the Q8R element, the peak pressure converges at a rate of about h^1, and the $B/16$ mesh is within about 10% of the extrapolated value. The width of the shear zone and the plastic dissipation are mesh-independent to within 5–10%. The numerical cohesion adds a term of about cN_c, which must be accounted for when the results are compared with solutions for cohesionless soil.

The internal length: regularisation or material parameter. For sand, shear bands are 10–20 grain diameters thick [17,18], which corresponds to a Cosserat length of the order of the grain size [22,49], about 0.1–1 mm for Karlsruhe fine sand ($d_{50} = 0.14$ mm). The values used here, $l = 25$–100 mm for $B = 1$ m, are two to three orders of magnitude larger. In the footing analyses, l is therefore a regularisation parameter chosen to be resolved by the mesh, and the computed band thickness (0.3–0.5 m, i.e., 5–12l) is not a physical property of the sand. Resolving the physical band width in a prototype footing would require elements of a fraction of a millimetre. The results show that this choice is not neutral. The peak pressure increases by about 7% per doubling of l/B in the range studied (Table 7), and in the shallow mechanism of the N_γ benchmark $l/B = 0.05$ adds about one third. In the slope example, the peak force increases by 5–11% per doubling of l and the post-peak force by up to 80% between $l = 0.05$ and 0.3 m (Figure 17b), whereas the regularisation stress δ has no effect for the values used (Section 3.3). The capacities computed with a regularising length should therefore be read as upper estimates of the capacity for $l \to 0$, which cannot be computed with the classical continuum because of mesh dependence. Quantitative statements on the Cosserat contribution to the scale effect of real footings require a physically identified l, e.g., from the band thickness in element tests [17,18] or from model footings of different size [15,51]. They also require meshes that resolve it, as in laboratory-scale analyses [51].

Classical versus Cosserat analyses. With softening, the classical continuum gives shear bands whose width is proportional to the element size (about two elements), so that the post-peak response, the band width and the dissipated energy depend on the mesh. The slope example shows this with an independent commercial code: in ANSYS, the force at $U = 100$ mm decreases from 453 to 234 kN/m between the coarse and the fine mesh, and the plastic strain in the band grows from 0.35 to 0.85; the present code gives the same mesh dependence for $l \to 0$. With an internal length resolved by the mesh, the load–settlement curves of the two finer meshes agree within 1.5% up to large settlements and the band width is fixed by l (Section 6). In the strip-footing problem, near-classical analyses stall shortly after the onset of localisation and cannot reach the peak (Section 5.3). The Cosserat model removes these problems at a moderate cost: three degrees of freedom per node instead of two, and a local return that is only slightly more complex. The full load–settlement curve, including the peak, the progressive mobilisation of strength and the post-peak response, can then be computed with a calibrated softening model. This is relevant for performance-based design, in which the settlement at the peak and the reserve capacity beyond it are of interest. The results also show the opposite risk. A regularised model on a coarse mesh of low-order elements can overestimate the collapse load by 20–40%, and the regularisation is effective only when the mesh resolves the internal length. Both mesh convergence and element performance must therefore be checked.

Small strains and mesh distortion. The analyses use a small-strain formulation up to $s/B = 20\%$. The distortion of the elements was evaluated from the deformed geometry of their corners. At $s/B = 10\%$, the largest change in an element angle is 42–54° and the largest area change 60–90% (Q8R, $h = B/16$, $l/B = 0.025$–0.1), both only in the elements at the footing edge. At the peak ($s/B \approx 15\%$), these elements are distorted by 56–75°, while those in the rest of the mechanism remain moderately deformed. The peak pressure and the mechanism are therefore governed by a region in which the small-strain approximation is acceptable, but the post-peak branch beyond $s/B \approx 15\%$ is affected by the strong distortion at the edge and should be read as qualitative. A large-deformation formulation with remeshing, or an arbitrary Lagrangian–Eulerian formulation as recently implemented for shallow foundations in granular media [12], would be required for a quantitative post-peak response [51].

Comparison with experiments. No model footing tests on Karlsruhe fine sand are available. The computed trends can be compared qualitatively with model tests on other dense sands [15,16]. Those tests show a rigid wedge beneath the footing, a peak at a settlement of several percent of B followed by softening, and a decrease in the normalised capacity with γB, all of which are reproduced by the analyses (Sections 5.9 and 5.11). A quantitative comparison would require a calibration on the sand used in those tests and is left to future work.

8. Conclusions

1. A plane-strain Cosserat Mohr–Coulomb model with a Rankine tension cut-off and hardening and softening of φ and ψ was formulated and implemented with a Fischer–Burmeister semismooth return and a consistent tangent. The point update converges quadratically on all tested multi-surface paths, the tangent agrees with finite differences within the expected truncation and round-off errors, the patch test is passed to round-off, and the implementation converges to the exact collapse loads of benchmark footing problems.
2. Calibrated on one drained triaxial test on dense Karlsruhe fine sand, the model predicts four further tests with full-curve errors of 3–5% in the deviator stress and 0.2–0.9% strain in the volumetric strain between 50 and 300 kPa, and peak errors below 4%. At 400 kPa the peak is overestimated by 15%, and the peak is reached at a smaller axial strain than measured, which is a limitation of the two-parameter hardening branch. Bolton's relation predicts the peaks within −4 to +7% in a leave-one-out test.
3. Low-order (Q4, B-bar) elements lock in the dilatant plastic flow and overestimate the capacity of the footing; this explains the high capacities and the mesh dependence obtained with this element. With eight-node elements, the peak pressure converges at a rate of about h^1 at fixed internal length, while the width of the shear zone and the plastic dissipation are mesh-independent within 5–10%. The numerical cohesion adds a term of about cN_c, which was quantified and removed by extrapolation.
4. The mesh-converged capacity for $l/B = 0.05$ is about 30% below the rigid–plastic solution for the peak friction angle and 30% above that for Davis' reduced angle. It increases by about 7% per doubling of l/B, so that the regularising internal length must be regarded as a parameter of the computed capacity.
5. The peak is reached at $s/B \approx 15$–16%. Maps of the mobilised friction and dilatancy angles show that the peak strength is mobilised progressively: at the peak, softening has started along the wedge boundary while the passive side is still hardening. The rigid wedge forms at 58–67°, close to the Prandtl value for the peak angle and far from Terzaghi's assumption $\alpha = \varphi$, while the mechanism reaches the surface at about 4–5B, much closer to the footing than the Prandtl mechanism of the peak angle.
6. Peak angles that depend on the current mean stress and void ratio reduce the capacity by 17% for $B = 1$ m and by 12–26% for $B = 0.5$–4 m. They cause a scale effect of 7–8% per doubling of B. With constant angles, the scale effect at the peak is about 2.5% per doubling and is explained by the stress-dependent stiffness, as shown by an analysis with $E/(\gamma B)$ kept constant.
7. For a rigid footing at the crest of a cohesive-frictional slope analysed on identical meshes, the present code reproduces the classical Mohr–Coulomb solution of ANSYS within 0.5–3% when the internal length is small. With cohesion softening, the classical solutions of both codes depend on the mesh: the peak decreases and the post-peak force drops earlier and faster on finer meshes, in a band whose width halves with each refinement (3.1, 1.6, 0.8 and 0.4 m); on the finest mesh the classical analysis cannot pass the peak without numerical stabilisation. With an internal length resolved by the mesh,

the load–settlement curves and the band width (about $15l$) are mesh-independent, while the failure mechanism is unchanged.

Author Contributions: Conceptualization, A.P.; methodology, A.P.; software, A.P.; validation, A.P.; formal analysis, A.P.; investigation, A.P.; data curation, A.P.; writing—original draft preparation, A.P.; writing—review and editing, A.P.; visualization, A.P.; supervision, A.H.A. All authors have read and agreed to the published version of the manuscript.

Funding: This research received no external funding.

Institutional Review Board Statement: Not applicable.

Informed Consent Statement: Not applicable.

Data Availability Statement: The data presented in this study are available on request from the corresponding author.

Conflicts of Interest: The authors declare no conflicts of interest.

Appendix A. Single-Element Comparison with ANSYS

A single eight-node element (1×1 m, plane strain) was loaded by a confining pressure of 50 kPa on one lateral face and by a uniform vertical displacement up to 5% axial strain, with the material of Section 6.1. Figure A1 compares the two codes. For perfect plasticity, the axial stress at failure is 166.354 kPa in both, and the out-of-plane stress 86.54 kPa. For the cohesion softening of case B (the table was extended here to a residual of 4 kPa at $\kappa = 0.36$ to make the softening visible), the ANSYS hardening variable back-calculated from the stress–strain curve equals 0.865 times its equivalent plastic strain and the accumulated plastic multiplier κ of the present model within 2%; the axial stresses agree within 0.1% up to 4% axial strain and within 1.4% at 5%.

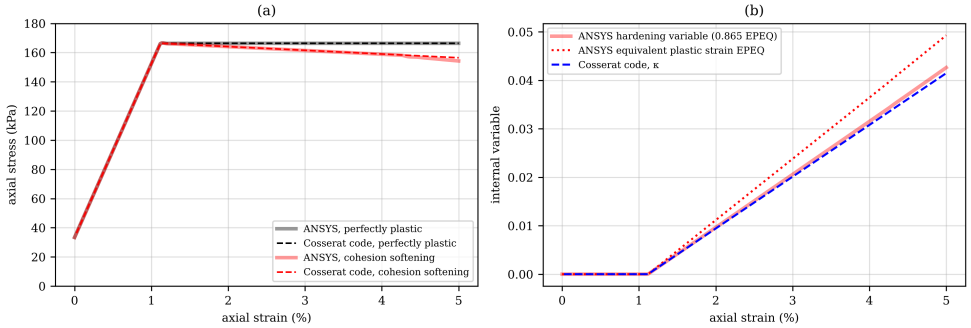

Figure A1. Single-element plane-strain compression ($\sigma_3 = 50$ kPa): (**a**) axial stress versus axial strain from ANSYS and from the Cosserat code, perfectly plastic and with cohesion softening; (**b**) internal variables.

Appendix B. Finite-Difference Verification of the Tangent

The choice of the finite-difference perturbation in Section 3.3 was checked by repeating the comparison for $h_r = 10^{-1} \ldots 10^{-11}$, with $h = h_r \max(10^{-6}, \|\boldsymbol{\varepsilon}\|)$, at seven representative converged states (Figure A2). Where the response is smooth, the error of the central difference decreases as h_r^2 and that of the one-sided differences as h_r, down to a minimum of 10^{-11}–10^{-10} at $h_r \approx 10^{-5}$–10^{-6}; for smaller perturbations it increases again, approximately as $1/h_r$, because of round-off and of the local tolerance of the return (10^{-10}). At the apex with the Rankine cut-off, where the local problem is less well conditioned, the minimum is 7×10^{-9}. For large perturbations, the perturbed state leaves the current active set, and the error remains of order 0.1–1 until the perturbation is smaller than the distance to the

neighbouring facet ($h_r \leq 10^{-5}$ for the edge state). At the kink of the uniaxial-extension path, the central and backward differences do not converge at all, whereas the forward difference converges linearly to the analytical tangent: the response is not differentiable there, and the analytical tangent is the one-sided tangent of the active set. The interval $h_r = 10^{-4} \ldots 10^{-9}$ used for Table 1 therefore lies where the truncation and round-off errors are smallest, and taking the smallest of the central, forward and backward errors identifies the correct one-sided tangent at kinks.

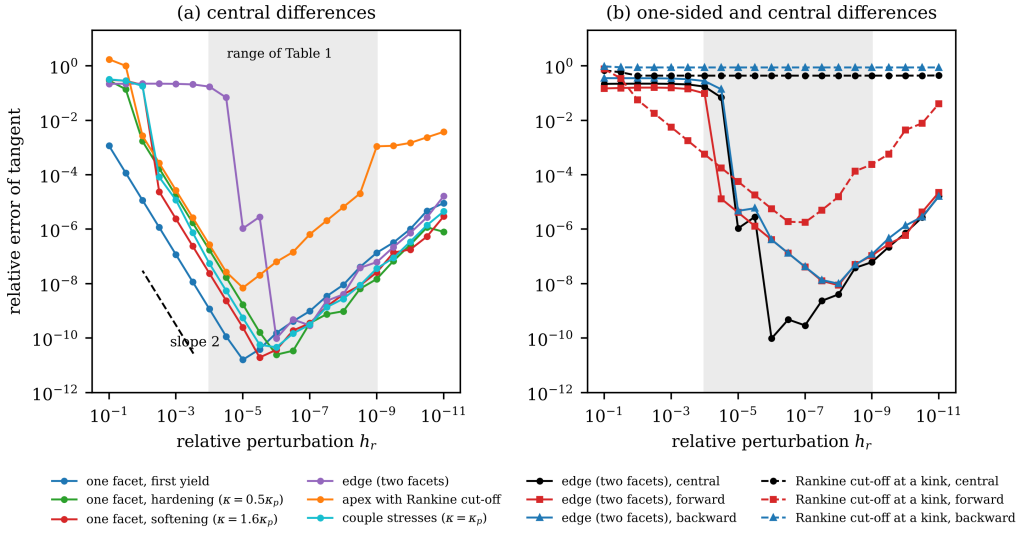

Figure A2. Finite-difference verification of the consistent tangent as a function of the relative perturbation h_r: (**a**) central differences at six converged states; (**b**) central, forward and backward differences at an edge state and at a kink of the Rankine cut-off. Shaded: interval used for Table 1.

References

1. Prandtl, L. Über die Härte plastischer Körper. *Nachrichten Von Der Ges. Der Wiss. Zu GÖTtingen Math.-Phys. Kl.* **1920**, *1920*, 74–85.
2. Terzaghi, K. *Theoretical Soil Mechanics*; John Wiley & Sons: New York, NY, USA, 1943.
3. Meyerhof, G. Some recent research on the bearing capacity of foundations. *Can. Geotech. J.* **1963**, *1*, 16–26. [CrossRef]
4. Vesić, A. Analysis of ultimate loads of shallow foundations. *J. Soil Mech. Found. Div.* **1973**, *99*, 45–73. [CrossRef]
5. Martin, C. Exact bearing capacity calculations using the method of characteristics. In Proceedings of the 11th International Conference of the International Association for Computer Methods and Advances in Geomechanics, Turin, Italy, 19–24 June 2005; Volume 4, pp. 441–450.
6. Lyamin, A.; Salgado, R.; Sloan, S.; Prezzi, M. Two- and three-dimensional bearing capacity of footings in sand. *Géotechnique* **2007**, *57*, 647–662. [CrossRef]
7. Loukidis, D.; Salgado, R. Bearing capacity of strip and circular footings in sand using finite elements. *Comput. Geotech.* **2009**, *36*, 871–879. [CrossRef]
8. Iqbal, T.; Ohtsuka, S.; Isobe, K.; Fukumoto, Y.; Kaneda, K. Modified ultimate bearing capacity formula of strip footing on sandy soils considering strength non-linearity depending on stress level. *Soils Found.* **2023**, *63*, 101325. [CrossRef]
9. Liang, W.; Zhao, S.; Wu, H.; Zhao, J. Bearing capacity and failure of footing on anisotropic soil: A multiscale perspective. *Comput. Geotech.* **2021**, *137*, 104279. [CrossRef]
10. Mase, L.Z.; Putri, M.A.; Edriani, A.F.; Lai, V.Q.; Keawsawasvong, S. Prediction of the Bearing Capacity of Strip Footing at the Homogenous Sandy Slope Based on the Finite Element Method and Multivariate Adaptive Regression Spline. *Transp. Infrastruct. Geotechnol.* **2023**, *11*, 1520–1546. [CrossRef]
11. Niebler, M.; Chrisopoulos, S.; Cudmani, R.; Rebstock, D. A General Framework to Simulate Soil–Structure Interface Behaviour Using Advanced Constitutive Models. *Modelling* **2025**, *6*, 11. [CrossRef]
12. Yosef, T.Y.; Fang, C.; Steelman, J.S.; Pajouh, M.A.; Faller, R.K.; Stolle, C.S.; Kim, S. Efficient hybrid FEM+ALE implementation for large deformation impact simulation of shallow foundations in granular media. *Adv. Eng. Softw.* **2026**, *220*, 104225. [CrossRef]
13. Rowe, P. The stress-dilatancy relation for static equilibrium of an assembly of particles in contact. *Proc. R. Soc. Lond. A* **1962**, *269*, 500–527. [CrossRef]

14. Bolton, M. The strength and dilatancy of sands. *Géotechnique* **1986**, *36*, 65–78. [CrossRef]
15. Tatsuoka, F.; Okahara, M.; Tanaka, T.; Tani, K.; Morimoto, T.; Siddiquee, M. Progressive failure and particle size effect in bearing capacity of a footing on sand. In Proceedings of the Geotechnical Engineering Congress, Geotechnical Special Publication No. 27, Boulder, CO, USA, 10–12 June 1991; pp. 788–802.
16. Siddiquee, M.; Tatsuoka, F.; Tanaka, T.; Tani, K.; Yoshida, K.; Morimoto, T. Model tests and FEM simulation of some factors affecting the bearing capacity of a footing on sand. *Soils Found.* **2001**, *41*, 53–76. [CrossRef] [PubMed]
17. Desrues, J.; Viggiani, G. Strain localization in sand: An overview of the experimental results obtained in Grenoble using stereophotogrammetry. *Int. J. Numer. Anal. Methods Geomech.* **2004**, *28*, 279–321. [CrossRef]
18. Rattez, H.; Shi, Y.; Sac-Morane, A.; Klaeyle, T.; Mielniczuk, B.; Veveakis, M. Effect of grain size distribution on the shear band thickness evolution in sand. *Géotechnique* **2022**, *72*, 350–363. [CrossRef]
19. Huang, Y.; Wang, T.; Guo, H.; Zhang, Y.; Hao, Z.; Lu, X.; Zhang, X. Initiation of Shear Band in Gas Hydrate-Bearing Sediment Considering the Effect of Porosity Change on Stress. *Modelling* **2025**, *6*, 51. [CrossRef]
20. de Borst, R. Simulation of strain localization: A reappraisal of the Cosserat continuum. *Eng. Comput.* **1991**, *8*, 317–332. [CrossRef]
21. Vardoulakis, I.; Sulem, J. *Bifurcation Analysis in Geomechanics*; Blackie Academic & Professional: London, UK, 1995.
22. Mühlhaus, H.; Vardoulakis, I. The thickness of shear bands in granular materials. *Géotechnique* **1987**, *37*, 271–283. [CrossRef]
23. Xue, D.; Lü, X.; Lim, K.W.; Buscarnera, G. Nonlocal implicit gradient enhancements for strain localization informed by controllability criteria for plastic solids. *Comput. Methods Appl. Mech. Eng.* **2023**, *415*, 116275. [CrossRef]
24. Liu, C.; Xia, X. A Modified Nonlocal Macro–Micro-Scale Damage Model for the Simulation of Hydraulic Fracturing. *Modelling* **2025**, *6*, 58. [CrossRef]
25. Yang, Q.; Lu, G.; Xia, X. Dynamic Simulation of Complex Multiple-Crack Evolution Under Blast Loading Using a Nonlocal Macro-Meso-Scale Consistent Damage Model. *Modelling* **2026**, *7*, 101. [CrossRef]
26. Zhou, H.; Shen, F.; Gu, X.; Li, B. Regularization effect of peridynamic horizon on strain localization and soil slope instability analysis. *Eng. Anal. Bound. Elem.* **2024**, *165*, 105774. [CrossRef]
27. Rødvand, L.A.; Jostad, H.P.; Grimstad, G.; Andresen, L. Modelling mesh independent failure loads of a soft strain-softening clay using a rate dependent model. *Comput. Geotech.* **2023**, *161*, 105512. [CrossRef]
28. Li, Y.; Tang, H.; Song, X.; Zhu, F.; Hu, Z. Regularization analysis of the strong discontinuity-Cosserat finite element method for modeling strain localization in cohesive-frictional materials by spectral theory. *Comput. Geotech.* **2023**, *162*, 105640. [CrossRef]
29. Schanz, T.; Vermeer, P.; Bonnier, P. The hardening soil model: Formulation and verification. In *Proceedings of the Beyond 2000 in Computational Geotechnics*; Brinkgreve, R., Ed.; Balkema: Rotterdam, The Netherlands, 1999; pp. 281–296.
30. Nagtegaal, J.C.; Parks, D.M.; Rice, J.R. On numerically accurate finite element solutions in the fully plastic range. *Comput. Methods Appl. Mech. Eng.* **1974**, *4*, 153–177. [CrossRef]
31. de Borst, R.; Vermeer, P.A. Possibilities and limitations of finite elements for limit analysis. *Géotechnique* **1984**, *34*, 199–210. [CrossRef]
32. Permanoon, A.; Akhaveissy, A.H. Failure of existing structures with semi-brittle mechanical properties on meso scale and reduction of computational cost using non-linear topology optimization. *Constr. Build. Mater.* **2022**, *319*, 126071. [CrossRef]
33. Khorami, N.; Nikkhoo, A.; Sadollah, A.; Permanoon, A.; Hejazi, F. Computational time reduction in meso-scale masonry structure analysis by nonlinear topology optimization methods. *Int. J. Civ. Eng.* **2025**, *23*, 1263–1286. [CrossRef]
34. Fattahi, M.; Malekshahi, M.; Permanoon, A. Mesoscale numerical modeling of unreinforced masonry wall response to underground dynamic loads: A comparative study utilizing FEM and DEM. *Structures* **2024**, *63*, 106460. [CrossRef]
35. Ye, X.; Wei, W.; Zhang, H.; Ji, Z.; Tang, H.; Zhao, X. Finite element analysis for pullout resistance and progressive failure of strip anchors in strain softening marine soils. *Sci. Rep.* **2025**, *15*, 5543. [CrossRef] [PubMed]
36. Ye, X.; Wei, W.; Ye, X.; Tang, H.; Ji, Z.; zhao, X. Envelope of bearing capacity for gravity anchors in strain-softening soils under VHM loading: A Cosserat continuum FEM study. *Appl. Ocean Res.* **2025**, *164*, 104766. [CrossRef]
37. Xie, J.; Yang, T.; He, G.; Feng, H.; Peng, T.; Zheng, H. Progressive Failure Characteristics of Strain-Softening Subgrade Slopes Based on the Local Slip Point Safety Factor. *CivilEng* **2026**, *7*, 57. [CrossRef]
38. Lin, R.; A, F.; Jia, H.; Luo, Z.; He, S.; Yan, S. Progressive Deformation Mechanism and Stability Analysis of a High-Fill Expansive Soil Slope. *Modelling* **2026**, *7*, 196. [CrossRef]
39. Cosserat, E.; Cosserat, F. *Théorie des Corps Déformables*; A. Hermann et Fils: Paris, France, 1909.
40. Arslan, H.; Sture, S. Finite element analysis of localization and micro–macro structure relation in granular materials. Part II: Implementation and simulations. *Acta Mech.* **2008**, *197*, 153–171. [CrossRef]
41. Godio, M.; Stefanou, I.; Sab, K.; Sulem, J. Multisurface plasticity for Cosserat materials: Plate element implementation and validation. *Int. J. Numer. Methods Eng.* **2016**, *108*, 456–484. [CrossRef]
42. de Borst, R.; Alizadeh Sabet, S.; Hageman, T. Non-associated Cosserat plasticity. *Int. J. Mech. Sci.* **2022**, *230*, 107535. [CrossRef]
43. Chang, J.; Li, S.; Wang, W.; Niu, Q. A study of non-coaxial effects on strain localization via micropolar plasticity model. *Acta Geotech.* **2022**, *17*, 721–739. [CrossRef]

44. Tang, J.b.; Chen, X.; Liu, Z.q.; Cui, L.s. Numerical Analysis of Strain Localization in Granular Soils by Modified Cam-Clay Model Based on Micropolar Continuum Theory. *Int. J. Geomech.* **2024**, *24*, 04024138. [CrossRef]
45. Wei, W.; Tang, H.; Liu, Y.; Chen, H. Cosserat model incorporating anisotropy evolution and its application in numerical analysis of strain localization in clay. *Acta Geotech.* **2024**, *20*, 365–385. [CrossRef]
46. Song, X.; Pashazad, H. Computational Cosserat periporomechanics for strain localization and cracking in deformable porous media. *Int. J. Solids Struct.* **2024**, *288*, 112593. [CrossRef]
47. Pan, Y.; Yang, D.; Chu, X.; Qu, W. Discrete element investigation into Cosserat effects of granular materials: The measurement of couple stress and Cosserat modulus. *Powder Technol.* **2024**, *435*, 119397. [CrossRef]
48. Wu, W.; Bauer, E.; Kolymbas, D. Hypoplastic constitutive model with critical state for granular materials. *Mech. Mater.* **1996**, *23*, 45–69. [CrossRef]
49. Tejchman, J.; Bauer, E. Numerical simulation of shear band formation with a polar hypoplastic constitutive model. *Comput. Geotech.* **1996**, *19*, 221–244. [CrossRef]
50. Herle, I.; Tejchman, J. A "class A" prediction of the bearing capacity of plane strain footings on sand. *Soils Found.* **1999**, *39*, 47–60. [CrossRef] [PubMed]
51. Tejchman, J.; Górski, J. Size effects in problems of footings on sand within micro-polar hypoplasticity. *Arch. Hydro-Eng. Environ. Mech.* **2008**, *55*, 95–124.
52. Panteghini, A.; Lagioia, R. A micropolar isotropic plasticity formulation for non associated flow rule and softening featuring multiple classical yield criteria. Part II—FE integration and applications. *arXiv* **2021**, arXiv:2106.12869.
53. Panteghini, A.; Rubin, M. Strain localization in softening plasticity without modifying standard constitutive models: A deformable Cosserat approach. *Int. J. Eng. Sci.* **2026**, *228*, 104638. [CrossRef]
54. Clausen, J.; Damkilde, L.; Andersen, L. An efficient return algorithm for non-associated plasticity with linear yield criteria in principal stress space. *Comput. Struct.* **2007**, *85*, 1795–1807. [CrossRef]
55. Simo, J.; Hughes, T. *Computational Inelasticity*; Springer: New York, NY, USA, 1998.
56. Fischer, A. A special Newton-type optimization method. *Optimization* **1992**, *24*, 269–284. [CrossRef]
57. Wichtmann, T.; Triantafyllidis, T. An experimental database for the development, calibration and verification of constitutive models for sand with focus to cyclic loading: Part I—tests with monotonic loading and stress cycles. *Acta Geotech.* **2016**, *11*, 739–761. [CrossRef]
58. Hardin, B.; Richart, F. Elastic wave velocities in granular soils. *J. Soil Mech. Found. Div.* **1963**, *89*, 33–65. [CrossRef]
59. Hughes, T. Generalization of selective integration procedures to anisotropic and nonlinear media. *Int. J. Numer. Methods Eng.* **1980**, *15*, 1413–1418. [CrossRef]
60. Terzi, V.G.; Makarios, T.K. Finite Element In-Depth Verification: Base Displacements of a Spherical Dome Loaded by Edge Forces and Moments. *Modelling* **2023**, *5*, 37–54. [CrossRef]
61. Knittel, L.; Tafili, M.; Tavera, C.G.; Triantafyllidis, T. New perspectives on preshearing history in granular soils. *Sci. Rep.* **2023**, *13*, 4576. [CrossRef] [PubMed]
62. Irani, N.; Duque, J.; Tafili, M.; Mašín, D.; Wichtmann, T. Influence of drainage conditions and monotonic preloadings on the monotonic behavior of Karlsruhe fine sand. *Acta Geotech.* **2025**, *20*, 4369–4383. [CrossRef]
63. Knudsen, B.S.; Mortensen, N. Bearing capacity, comparison of results from FEM and DS/EN 1997-1 DK NA 2013. In Proceedings of the 17th Nordic Geotechnical Meeting, Reykjavik, Iceland, 25–28 May 2016.
64. Hansen, J. A revised and extended formula for bearing capacity. *Dan. Geotech. Inst. Bull.* **1970**, *28*, 5–11.
65. *EN 1997-1:2004;* Eurocode 7: Geotechnical Design—Part 1: General Rules. European Committee for Standardization: Brussels, Belgium, 2004.

Disclaimer/Publisher's Note: The statements, opinions and data contained in all publications are solely those of the individual author(s) and contributor(s) and not of MDPI and/or the editor(s). MDPI and/or the editor(s) disclaim responsibility for any injury to people or property resulting from any ideas, methods, instructions or products referred to in the content.